1 Measurement Report: Characterization of Aerosol Hygroscopicity over Southeast Asia during
2 the NASA CAMP[2]Ex Campaign

3 Genevieve Rose Lorenzo[1,2], Luke D. Ziemba[3], Avelino F. Arellano[1], Mary C. Barth[4], Ewan C.
4 Crosbie[3,5], Joshua P. DiGangi[3], Glenn S. Diskin[3], Richard Ferrare[3], Miguel Ricardo A. Hilario[1],
5 Michael A. Shook[3], Simone Tilmes[4], Jian Wang[6], Qian Xiao[6], Jun Zhang[4], and Armin
6 Sorooshian[1,7]

7 [1]Department of Hydrology and Atmospheric Sciences, University of Arizona, Tucson, Arizona,
8 85721, USA
9 [2]Manila Observatory, Quezon City, 1108, Philippines
10 [3]NASA Langley Research Center, Hampton, Virginia, 23681 USA
11 [4]Atmospheric Chemistry Observations & Modeling Laboratory, NSF National Center for
12 Atmospheric Research, Boulder, Colorado, 80301, USA
13 [5]Analytical Mechanics Associates, Inc, Hampton, Virginia, 23666 USA
14 [6]Department of Energy, Environmental & Chemical Engineering, Washington University in St
15 Louis, St. Louis, Missouri, 63130, USA
16 [7]Department of Chemical and Environmental Engineering, University of Arizona, Tucson,
17 Arizona, 85721, USA

18 *Correspondence to: armin@arizona.edu*

19 **Abstract**

20 This study characterizes the spatial and vertical nature of aerosol hygroscopicity in Southeast Asia
21 and relates it to aerosol composition and sources. Aerosol hygroscopicity via the light scattering
22 hygroscopic growth factor, f(RH), is calculated from the amplification of PM_5 aerosol ($D_p < 5$ µm)
23 scattering measurements from < 40% to 82% relative humidity during the Cloud, Aerosol, and
24 Monsoon Processes Philippines Experiment (CAMP[2]Ex) between August to October 2019 over
25 the northwest tropical Pacific. Median f(RH) is relatively low (1.26 with lower to upper quartiles
26 of 1.05 to 1.43) like polluted environments, due to the dominance of the mixture of organic carbon
27 and elemental carbon. The f(RH) is lowest due to smoke from the Maritime Continent (MC)
28 during its peak biomass burning season, coincident with high carbon monoxide concentrations (>
29 0.25 ppm) and pronounced levels of accumulation mode particles and organic mass fractions. The
30 highest f(RH) values are linked to coarser particles from the West Pacific and aged biomass
31 burning particles in the region farthest away from the MC, where f(RH) values are lower than
32 typical polluted marine environments. Convective transport and associated cloud processing in
33 these regions decrease and increase hygroscopicity aloft in cases with transported air masses
34 exhibiting increased organic and sulfate mass fractions, respectively. An evaluation of a global
35 chemical transport model (CAM-chem) for cases of vertical transport showed the
36 underrepresentation of organics resulting in overestimated modeled aerosol hygroscopicity. These
37 findings on aerosol hygroscopicity can help to improve aerosol representation in models and the
38 understanding of cloud formation.

39

1. Introduction

Aerosol particles affect climate and visibility through the direct and indirect extinction of solar radiation via absorption and scattering of light and through cloud formation, respectively. Aerosol hygroscopicity compounds aerosol effects on Earth's radiation budget (Zhao et al., 2018; Malm and Day, 2001), secondary aerosol formation and cloud formation (Köhler, 1936), and health (Dockery, 2001). Neglecting the effect of moisture on aerosol growth leads to incorrect estimation of the cooling at Earth's surface due to aerosol particles (Garland et al., 2007). For instance, a decrease in light extinction over the southeast U.S. was linked to reduced aerosol water uptake, coincident with decreases in the sulfate/organic ratio (Attwood et al., 2014). Particle aging/coating can cause underestimation of both aerosol hygroscopicity in the sub-saturated regime (Wang et al., 2018) and cloud condensation nuclei (CCN) activity in the supersaturated regime for aged particles in China by ~22% (Zhang et al., 2017). Remote sensing of aerosol optical properties is also affected by aerosol water content (Ferrare et al., 1998; Ferrare et al., 2023). Therefore, accurate aerosol hygroscopicity values are critical for remote sensing and satellite observation of aerosol particles (Ziemba et al., 2013; van Diedenhoven et al., 2022).

Aerosol hygroscopicity is described by physical quantities such as the diameter growth factor, g(RH), and light scattering hygroscopic growth factor, f(RH). The g(RH) parameter relates the wet particle diameter of the aerosol at a high relative humidity to the dry diameter of the aerosol at low relative humidity, while f(RH) relates total scattering due to the aerosol at high relative humidity (80%) to that at low relative humidity (<40%) (Waggoner et al., 1983; Hegg et al., 1993). Light scattering increases with relative humidity for most particles and is correlated to chemical composition and size (Baynard et al., 2006; Swietlicki et al., 2008) of particulate matter (Covert et al., 1972; Brock et al., 2016a).

Direct measurement of aerosol hygroscopicity, however, is difficult and is also not well-represented in climate models (Chen et al., 2014). The hygroscopicity parameter kappa, κ, is a single parameter that was developed to represent water uptake in models. It determines the volume (or mass or moles, with appropriate unit conversions) of water that is associated with a unit volume of a dry aerosol particle (Petters and Kreidenweis, 2007). A simple and commonly used water uptake model for calculating kappa is based on the Zdanovskii, Stokes and Robinson (ZSR) treatment for water soluble organic-inorganic mixed aerosol particles (Stokes and Robinson, 1966) where it is assumed that there are no interactions between the organic and inorganic species. In the ZSR model, water uptake of the individual non-interacting components can be summed up linearly to represent the total water uptake of the mixed aerosol. The interaction of organics and inorganics, however, along with the aging-specific density of organics is thought to influence hygroscopicity and affect both the ZSR calculation (Fan et al., 2020) and aerosol particle growth factor via changes in molecular structure, molecular weight, functionality, and/or other properties (Swietlicki et al., 2008).

77   Observed and simulated aerosol hygroscopicity using aforementioned parameters are greater in
78   clean marine air masses compared to air masses over land, near terrestrial biogenic sources which
79   are secondary organics precursors, and under polluted conditions (Swietlicki et al., 2008; Duplissy
80   et al., 2011; Petters and Kreidenweis, 2007). In marine areas, hygroscopicity typically decreases
81   with altitude with decreasing inorganic fractions (Pringle et al., 2010). Cloud processing over
82   marine areas has been observed to increase the oxidation of organic aerosols (Che et al., 2022;
83   Dadashazar et al., 2022) and hygroscopicity in general (Crumeyrolle et al., 2008). Continental
84   aerosol particles have smaller diameters and are usually less hygroscopic due to more organic-rich
85   aerosol particles and pure elemental carbon (EC) particles (Wang et al., 2014; Kreidenweis and
86   Asa-Awuku, 2014). Organics are generally less hygroscopic than inorganics, and their
87   hygroscopicity is affected by oxidation level (e.g., O:C ratio), oxidation state, and solubility (Brock
88   et al., 2016a; Wu et al., 2016; Thalman et al., 2017). Aging has also been found to increase aerosol
89   hygroscopicity through the oxidation of secondary organic aerosols and organic aerosol
90   interactions with inorganics (Engelhart et al., 2008; Liu et al., 2014; Saxena et al., 1995).

91   Although aerosol studies in the rapidly developing Southeast Asia (SEA) region are increasing,
92   few are focused on the nature of aerosol particles and their interactions with water vapor and clouds
93   (Tsay et al., 2013; Ross et al., 2018; Reid et al., 2023). Understanding the interactions between
94   aerosols and the complex geographic, meteorological, and hydrological environment in Southeast
95   Asia remains challenging due to a still growing observational database, prevalence of clouds
96   interfering with remote sensing, and limited modeling studies (Tsay et al., 2013; Lee et al., 2018;
97   Chen et al., 2020; Hong and Di Girolamo, 2020; Amnuaylojaroen, 2023). This, along with
98   increased local and transported emissions and prevalent moisture-rich conditions in the region,
99   altogether motivate the need to understand aerosol hygroscopicity and associated impacts on
100   radiative transfer and on climate (Brock et al., 2016a; Ziemba et al., 2013). How freshly emitted
101   nearly hydrophobic particles transform into hygroscopic aerosol particles (Swietlicki et al., 2008),
102   for example, is an understudied topic in Southeast Asia where there are significant sources of
103   particles with low hygroscopicity (Reid et al., 2023). Understanding aerosol hygroscopicity will
104   also help in the need to improve remote sensing measurements in the region, which is affected by
105   overlapping high and low level clouds (Burgos et al., 2019; Hong and Di Girolamo, 2020).

106   Predicting aerosol hygroscopicity, especially at higher relative humidity (RH), is especially
107   difficult due to optical instruments underestimating particle light scattering at high RH and
108   mechanisms other than hygroscopicity impacting particle growth (Gasparini et al., 2006; Mochida
109   et al., 2006). This is important because atmospheric water content is high in Southeast Asia. For
110   example, the hygroscopicity of secondarily formed organics (via gas-to-particle conversion) is
111   found to be dependent on oxidation state for high RH (Shi et al., 2022). Southeast Asia has elevated
112   levels of organics, inorganics, and elemental carbon (Cruz et al., 2019; AzadiAghdam et al., 2019;
113   Oanh et al., 2006), allowing for an opportunity to see how hygroscopicity responds to a range of

114 relative values of each of these elevated components. Therefore, relating aerosol particle
115 composition to hygroscopicity, for closure (Xu et al., 2020), is particularly significant there.

116 Aerosol hygroscopicity is a crucial factor in the understanding and modeling of aerosol-cloud
117 interactions, because of the role hygroscopicity plays in cloud drop activation. The NASA Cloud,
118 Aerosol, and Monsoon Processes Philippines Experiment (CAMP^{2}Ex) was designed to understand
119 the role of aerosol particles in cloud formation and in regulating solar radiation during the
120 southwest monsoon (Reid et al., 2023). CAMP^{2}Ex occurred between August and October 2019
121 over the Philippines and neighboring areas. That campaign provides an aircraft dataset with
122 measurements focused on aerosol and cloud properties, which affords a valuable opportunity to
123 evaluate models with these measurements for shallow to moderate convection, which is one of the
124 biggest challenges for regional and global-scale atmosphere models to represent because these
125 clouds are much smaller than the model grid spacing.

126 In the CAMP^{2}Ex region, biomass burning aerosol hygroscopicity is over-estimated by global
127 atmosphere models simulating the CAMP2Ex campaign, with both the model size representation
128 of the aerosol particles and the size discrepancy between model and observations contributing to
129 this (Collow et al., 2022; Edwards et al., 2022). This overestimation can affect the representation
130 of clouds in the region. Clouds, especially shallow cumulus clouds, like those in the tropical West
131 Pacific (which the CAMP^{2}Ex region is part of) have been underestimated by models due to the
132 lack of observational data to improve convective parameterizations (Chandra et al., 2015). Part of
133 the challenge in modeling aerosol-cloud interactions is the ability to both have a high-resolution
134 representation, at the scale of the shallow convection, in a large enough domain, which is important
135 for understanding climatic effects to properly account for the bulk behavior of cloud fields (Spill
136 et al., 2019). This could be addressed by evolving modeling infrastructures, with higher resolution
137 schemes ranging from regional to convective scale within a larger domain (Pfister et al., 2020;
138 Radtke et al., 2021).

139 Knowledge gaps identified above are addressed in this study using the opportune CAMP^{2}Ex
140 dataset. To our knowledge, this is the first time this dataset has been explored extensively to
141 characterize aerosol hygroscopicity properties in the region. The goals of this proposed study are
142 to (i) characterize the spatial distribution of aerosol hygroscopicity in Southeast Asia during the
143 CAMP^{2}Ex airborne mission, (ii) relate aerosol hygroscopicity and composition, (iii) identify
144 emission events that impact aerosol hygroscopic growth, and (iv) evaluate a global chemical
145 transport model for aerosol vertical transport.
146
147 **2. Methods**

148 **2.1 CAMP^{2}Ex Field Campaign**

149 CAMP^{2}Ex included 19 research flights with a NASA P3 from 24 August to 5 October 2019.
150 Twelve of these flights were associated with the southwest monsoon (SWM) followed by a flow

151 reversal with seven flights conducted during the northeast monsoon (NEM) (Reid et al., 2023). As
152 summarized by Reid et al. (2023), the combination of airborne and ship-based measurements helps
153 to characterize interactions between various aerosol particle sources (e.g., biomass burning,
154 industrial, natural) and small to congestus convection. Below we note the P3 instruments most
155 relevant to this study.

156 **2.2 Observations and Derived Quantities**

157 **2.2.1 P3 Instrumentation**

158 As summarized in Table 1, data are used from a variety of aerosol particle and trace gas
159 instrumentation. The aerosol particle scattering and absorption instruments measure the optical
160 properties of bulk aerosol particles (PM_5): < 5 µm dry diameter (McNaughton et al., 2007). Aerosol
161 composition and size data for submicron particles were considered when they were collected using
162 a forward-facing shrouded isokinetic inlet. Non-refractory species in the submicron range studied
163 using an aerosol mass spectrometer (AMS) included sulfate, nitrate, ammonium, organics, and
164 chloride. We also use the ratio of the mass spectral marker m/z 44 marker relative to total organic
165 mass, f_{44}, as a possible indicator of air mass age. Submicron refractory species of black carbon
166 (also referred to as elemental carbon) from a single particle poot photometer (SP2) were also
167 included in the study. Bulk water-soluble aerosol particles were collected using a particle-into-
168 liquid sampler (PILS) that was analyzed using ion chromatography; species quantified included
169 oxalate, NH_4^+, dimethylamine (DMA), K^+, SO_4^{2-}, Ca^{2+}, Na^+, Mg^{2+}, Cl^-, NO_3^-, Br^-, and NO^-. Cloud-
170 free conditions were identified to ensure the highest quality aerosol data using a cloud flag product
171 based on measurements from the fast cloud droplet probe (FCDP) and two-dimensional stereo
172 probe (2DS). Aerosol particle composition data were considered for those cases when the total
173 aerosol non-refractory particle mass was greater than 0.4 µg sm^{-3}.

174 **Table 1:** Summary of instrument data used in this work.

Parameter	Instrument	Time Resolution	Uncertainty	Sampled Aerosol Particle Size	Reference
Latitude, Longitude, and Altitude	Northrop Grumman Litton 251 EGI	1 s	~5 m spherical error probable; 0.01°	N/A	Reid et al., 2023
Dry (RH < 40%) and humidified (RH = 80%)) light scattering coefficient (λ = 450, 550, 700 nm)	Parallel humidified TSI 3563 Nephelometers	1 s	30%	< 5μm diameter	Ziemba et al., 2013; McNaughton et al., 2007
Dry (RH < 40%) light absorption coefficient (λ = 470, 532, 660 nm)	Radiance Research 3 Particle Soot Absorption Photometer (PSAP)	1 s	15%	< 5μm diameter	Mason et al., 2018; McNaughton et al., 2007
Non-refractory aerosol (Organics, SO_4, NO_3, NH_4, Cl) mass concentration	Aerodyne High-Resolution Time-of-Flight Mass Spectrometer (AMS)	25 s	LLOD (μg sm^{-3}): Organics, 0.169; SO_4, 0.039; NO_3, 0.035; NH_4, 0.169; Cl, 0.036; Uncertainty: 50%	approximate relevant size range is 60-600 nm vac. aero. diameter	DeCarlo et al., 2008
Water-soluble mass concentration	Particle-into-liquid sampler (PILS) followed by offline ion chromatography analysis	238 s	30%	< 5μm diameter	Sorooshian et al., 2006 Crosbie et al., 2020
Refractory black carbon (BC) mass concentration	Single Particle Soot Photometer (DMT SP2)	1 s	10%	100 - 700 nm diameter	Schwarz et al., 2006
CO concentration	Picarro G2401-m	1 s	5 ppb	N/A	DiGangi et al., 2021
Volume and number concentration of particles	TSI Laser Aerosol Spectrometer (LAS) Model 3340	1 s	20%	0.1 - 5 μm optical diameter	Moore et al., 2021
Volume size distribution	Fast integrated mobility spectrometer (FIMS)	1 s	Concentration: 15%; Size: 3%	10 – 500 nm mobility diameter	Kulkarni and Wang, 2006; Wang et al., 2017; 2018

Cloud particles	SPEC-Hawkeye FCDP	1 s	50%	2 – 50 µm diameter	Knollenberg 1981, Lawson et al. 2017; Woods et al. 2018
Cloud particles	SPEC-Hawkeye 2DS	1 s	20%	10 µm – 3 mm diameter	Lawson et al. 2006a, Woods et al. 2018

175

2.2.2 Aerosol Hygroscopicity, f(RH), and Other Aerosol Optical Properties

176

177 Aerosol hygroscopicity is reported using the parameter f(RH), which is unitless and is the
178 amplification factor in scattering due to a change in RH. The f(RH) parameter is calculated from
179 the empirically derived exponential fit coefficient, gamma (γ), at 20% (RH_{dry}) and 80% (RH_{wet})
180 relative humidity (Ziemba et al., 2013). The gamma parameter is based on measurements of
181 scattering at 550 nm at two different relative humidity levels: dry ($< 40\%$) and humidified
182 (controlled to $82 \pm 10\%$). Gamma (Eq. 1) was calculated for times where the dry (SC_{dry}) and
183 humidified (SC_{wet}) scattering coefficients (Table 1) are greater than or equal to 5 Mm^{-1}. The f(RH)
184 (Eq. 2) was then derived from γ (Hänel, 1976).

185

186
$$\gamma = \frac{\ln \frac{SC_{wet}}{SC_{dry}}}{\ln \frac{100 - RH_{dry}}{100 - RH_{wet}}} \tag{1}$$

187
$$f(RH) = (\frac{100 - RH_{wet}}{100 - RH_{dry}})^{-\gamma} \tag{2}$$

188 All nephelometer scattering coefficient measurements were corrected for truncation errors using
189 the Anderson and Ogren's method (Anderson and Ogren, 1998). Relative humidity measurements
190 for the calculation of f(RH) were calibrated in the laboratory using nebulized ammonium sulfate
191 deliquescence at 80% (Brooks et al., 2002). System response is verified in flight by introducing
192 hydrophobic polystyrene latex spheres into the sample stream to ensure an f(RH) value of 1.0 is
193 observed. Absorption measurements were corrected for a variety of errors using the method from
194 Virkkula (2010) (Virkkula, 2010). Note that sampling efficiency decreases for supermicron
195 diameter particles with increasing size up to the 5-µm inlet cutoff, due to losses in transport tubing
196 and in the drying/humidification control system. Thus, derived f(RH) is applicable to
197 accumulation-mode particles and is partially sensitive to coarse-mode particles from 1-5 µm
198 diameter.

199

200 Single scattering albedo (SSA) was calculated when both the scattering and absorption coefficients
201 (smoothed with 30 s running average) were greater than 2 Mm^{-1}. The Ångström exponent (AE)
202 was calculated using the smoothed 30 s running average of the scattering and absorption
203 coefficients. The scattering Ångström exponent (SAE, 450-700 nm) was computed when the
204 scattering coefficient was greater than 2 Mm^{-1} based on Ziemba et al. (2013) and the absorption

205   Ångström exponent (AAE, 470-660 nm) was computed when the absorption coefficient was
206   greater than 2 Mm^{-1} (Mason et al., 2018).
207
208   **2.2.3 Sea Salt**
209   Bulk sea salt mass concentration was calculated using summed PILS concentrations of Na^+, Cl^-,
210   and Mg^{2+} along with the respective concentrations of the mass concentrations of K^+, Ca^{2+} and
211   SO_4^{2-} in sea salt (0.037, 0.04 and 0.25, respectively, by mass) (Crosbie et al., 2022).
212
213   **2.2.4 Aerosol Particle Classification**
214   Aerosol particle optical data were grouped depending on their AAE and SAE (Section 2.2.2)
215   values and based on the method of Cazorla et al. (2013), which used sun photometer measurements
216   to arrive at the following classifications as part of evaluating aircraft data over California, USA:
217   coated large particles, dust and elemental carbon mix, dust dominated, organic carbon and dust
218   mix, organic carbon dominated, elemental carbon and organic carbon mix, mixed, and elemental
219   carbon dominated. This method has been used for cases when chemical composition is not
220   available (Höpner et al., 2019), and can be useful because the composition data from the AMS is
221   limited to submicron particles (0.06 to 0.6 µm vacuum aerodynamic diameter) while the f(RH)
222   includes relatively larger particles (< 5 µm dry diameter).
223
224   **2.2.5 Effective Particle Density**
225   Following Shingler et al. (Shingler et al., 2016b), effective particle density was calculated by
226   dividing the sum of the 30 s total mass concentration from the AMS species (organics, SO_4^{2-}, NO_3^-
227   , NH_4^+, and Cl^-) and 30 s averaged black carbon from SP2 by the 30 s averaged integrated (for
228   particles with diameter from 0.1 to 1 µm) volume concentration from the LAS (Table 1).
229
230   **2.3 Modeling**
231
232   **2.3.1 Trajectory Analysis**
233   This work leverages trajectory results explained in detail by Hilario et al. (2021). This data product
234   associates air masses undergoing long-range transport nearby from the Maritime Continent (MC),
235   East Asia (EA), peninsular Southeast Asia (PSEA), and the West Pacific (WP) with specific
236   CAMP²Ex flight locations, where air masses were within the regions at altitudes below 2 km for
237   more than 6 h. The source regions are approximately within the following lowest and highest
238   latitude and longitude values, respectively: MC (-9.5º - 6.5º and 95º - 119º), EA (22º - 47º and 105º
239   - 121.5º), PSEA (10º - 20º and 98º - 106 º), and WP (3º-25º and 120.5º-122.5º). The National
240   Oceanic and Atmospheric Administration Hybrid Single Particle Lagrangian Integrated Trajectory
241   Model (HYSPLIT) (Stein et al., 2015; Rolph et al., 2017) was used to produce 5-day back
242   trajectories. The classification "Other" was used for back trajectories that either passed by the
243   regions but at elevations above the boundary layer (defined as 2 km), came from sources farther
244   away than the four listed above, were more localized to the Philippines, had too few sample counts,
245   or were from stagnant air (Hilario et al., 2021).
246

2.3.2 CAM-chem Model Configuration

247
248 The Community Atmosphere Model with comprehensive tropospheric and stratospheric chemistry
249 CAM-chem is used here as the atmospheric component of the Community Earth System Model
250 (CESM2). CAM-chem includes the modal aerosol model (MAM4) (Liu et al., 2016) and results
251 were evaluated with the CAMP²Ex AMS composition and f(RH) observations for two case studies.
252 Two CAM-chem simulations with different horizontal resolutions have been performed using the
253 spectral element grid mesh and dynamical core. The grid mesh resolution for one simulation was
254 uniform with ~111 km (labeled ne30). The other simulation employed regional refinement over
255 East Asia with grid spacing ~27 km (labeled MUSICA) in the regionally refined region and ~111
256 km elsewhere across the globe; a configuration as part of the Multi-Scale Infrastructure for
257 Chemistry and Aerosols version 0 (MUSICAv0) (Schwantes et al., 2022). More information about
258 CAM-chem is in the supplementary section (S1).

259

260 In CAM-chem, aerosol hygroscopicity is represented with the kappa value (Petters and
261 Kreidenweis, 2007) using the mixing rule (Stokes and Robinson, 1966). Kappa is calculated from
262 the CAM-chem Aitken (0.015 – 0.053 µm) and accumulation mode (0.058 – 0.48 µm) outputs
263 based on the volume fractions of the aerosol constituents (ε, Eq. 3) that was derived from their
264 densities (Table S1). The following internally mixed aerosol species from CAM-chem were
265 included in the analysis: organics (primary/hydrophobic, aged/hygroscopic, and secondary
266 ($C_{15}H_{38}O_2$)), sulfate (NH_4HSO_4), sea salt, dust ($AlSiO_5$), and black carbon (primary/hydrophobic
267 and aged/hygroscopic) (Tilmes et al., 2023). Some limitations in the calculation of kappa are that
268 CAM-chem does not include nitrate aerosol, and that constant kappa values for primary and aged
269 organics based on past work (Table S1) were used, even if it is known that kappa of organics varies
270 with aging (Kuang et al., 2020). Kappa was also calculated from the submicron AMS and SP2
271 observations using the assigned species properties for available aerosol species: aged organics,
272 aged black carbon, and ammonium sulfate. Submicron sea salt and dust data are not available and
273 were not included in the calculation for submicron kappa from observations.

274

275 $$\kappa_{chem} = \sum \kappa_i \, \varepsilon_i \qquad (3)$$

276

277 To enable a corresponding evaluation based on actual aerosol hygroscopicity observations, the
278 f(RH) from CAMP²Ex were converted to kappa based on past studies (Brock et al., 2016b; Kuang
279 et al., 2017; van Diedenhoven et al., 2022). The wet (80%) and dry (20%) relative humidity values
280 of the scattering measurements were used to convert f(RH) to an optical kappa (κ_{opt}) based on
281 Equation 4 (Brock et al., 2016b; Kuang et al., 2017). This was approximated from the proportional
282 relationship between the aerosol scattering cross section (which is the basis of f(RH)) and aerosol
283 volume (the change of which is usually described as growth factor) which Brock et al. (2016b) in
284 their study had associated with kappa. The optical kappa was converted to the chemical kappa
285 (κ_{chem}) based on the slope of the relationship between κ_{opt} and κ_{chem} from Brock et al. (2016b). This
286 method (Eq. 5) of converting κ_{opt} to κ_{chem} was also used by van Diedenhoven et al. (2022) for the
287 f(RH) data for CAMP²Ex and is associated with 40% uncertainty (van Diedenhoven et al., 2022).

288 The derived chemical kappa values for bulk aerosol particles are compared to the kappa calculated
289 using the ZSR mixing rule from the submicron observations (AMS and SP2) and model outputs.
290

291
$$f(RH) = \frac{1 + \kappa_{opt}\frac{RH_{wet}}{100 - RH_{wet}}}{1 + \kappa_{opt}\frac{RH_{dry}}{100 - RH_{dry}}}$$
(4)

292
$$\kappa_{chem} \approx \frac{\kappa_{opt}}{0.56}$$
(5)

293 **3. Results and Discussion**

294 **3.1 General Characterization of f(RH) for CAMP²Ex**

295 **3.1.1 Spatial and Vertical Distribution of f(RH)**

296 The f(RH) values in the CAMP²Ex campaign (Fig. 1a) were relatively low (median of 1.24 for
297 143,107 1 s points) with a narrow range of values (25th percentile (Q1) of 1.05 and 75th percentile
298 (Q3) of 1.42). The distribution of f(RH) and ambient RH values is narrowest in the lowest altitudes
299 (< 3 km), where most of the samples were taken (Fig. 1b). Both f(RH) and RH distributions become
300 broader at higher altitudes, where there is a higher prevalence also for higher f(RH) values and
301 lower RH values. Broadening of the f(RH) distribution at higher altitudes is at least partially
302 attributed to lower dry scattering coefficients that result in increased uncertainty in the calculation
303 of f(RH). The different aerosol sources (Fig. 1a) in the region also contribute to the range of
304 measured f(RH), with transported emissions from more distant sources presumably more
305 influential at the highest altitude ranges.
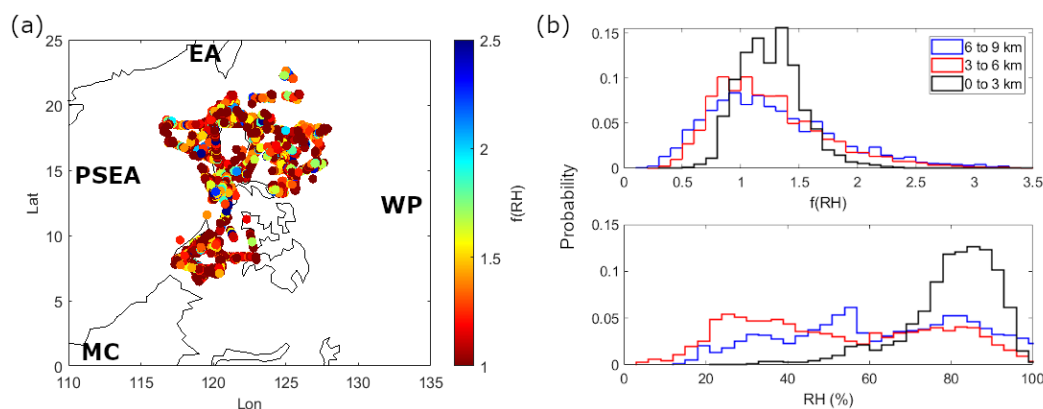
306

307 Figure 1. (a) Map showing f(RH) 1 s values along the CAMP²Ex flight paths with approximate locations and air mass
308 sources: Maritime Continent (MC), East Asia (EA), peninsular Southeast Asia (PSEA), and the West Pacific (WP)
309 (PSEA is farther west at ~105°E and EA extends farther north) of air mass sources (Hilario et al., 2021) around the
310 region. (b) Histograms of f(RH) and relative humidity (RH) for three altitude bins with the following counts: $n_{(0\ to\ 3}$
311 $_{km)}$: 139,026, $n_{(3\ to\ 6\ km)}$: 10,321, and $n_{(6\ to\ 9\ km)}$: 7,260.

312 The lowest median f(RH) (1.05 with Q1 and Q3 of 0.94 and 1.2) is from air masses traced to the
313 MC (Fig. 2a), which coincide with influence from smoke particles. The air mass from EA (Fig.

314   2a) has the narrowest range of values (Q1: 1.28, median (Q2): 1.38, Q3: 1.47), likely representative
315   of urban aerosol particles. The highest median f(RH) (1.49 with Q1 and Q3 of 1.26 of 1.73) are
316   from air masses with back trajectories from the WP (Fig. 2a), likely due to marine aerosol particles
317   interacting with particles from the MC and other regional sources. This mixing of the otherwise
318   clean marine air with regional pollution sources effectively decreases aerosol hygroscopicity and
319   this type of environment is often called a polluted marine environment (Titos et al., 2021).

320   Most (98%) of the f(RH) data were calculated for observations below 3 km (Fig. 2b), due to the
321   relatively clean free troposphere in the region. Median f(RH) values generally decrease with
322   altitude in the lower 3 km. An increase in median f(RH) is observed between 4 – 6 km (median
323   from 1.14 to 1.32), where the contribution of the mixed air mass ("Other") is most dominant. The
324   f(RH) values decrease above 6 km to the lowest median f(RH) (1.07) between 8 – 9 km, where air
325   masses are generally from Other and the MC.

326   Latitudinally (Fig. 2c), f(RH) is lowest nearest Borneo in the MC (median of 0.95 to 1.07 in the
327   regions from 6.85° N – 10.25° N), coincident with the dominant influence of biomass burning.
328   There were active fires in the area during the time samples were taken from this latitude. f(RH) is
329   highest in the northern Philippines (median of 1.33 to 1.44 in the regions from 18.75° N – 22.15°
330   N), where the influence of WP and EA air was most prevalent. This is consistent with the longitude
331   data (Fig. 2d), which exhibit the lowest f(RH) values for longitudes (median of 1.02 to 1.18 in the
332   regions from 117.95° E – 120.55° E) that had the highest MC contribution. The highest f(RH) is
333   observed in longitudes (median of 1.38 to 1.40 in the regions west of 116.65° E and east of 123.15°
334   E) that were more associated with the northern Philippines (Fig. 1a). To delve deeper into our
335   analysis, we discuss next the size and composition data.

336
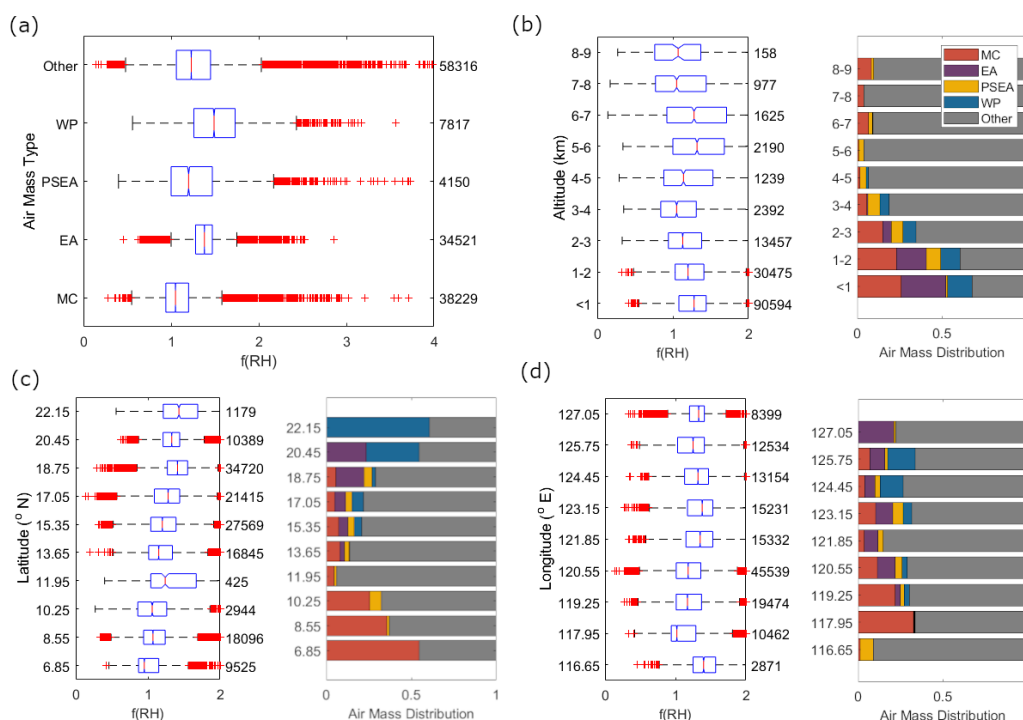
Figure 2. Distribution of 1 s f(RH) data during the CAMP²Ex field campaign for relevant (a) air masses, (b) altitude, (c) latitude, and (d) longitude levels and corresponding stacked bars of air mass contributions for panels b - d. The (a) air mass types are from Hilario et al. (2021). The numbers to the right of the notched boxplots are the counts, and the (b – d) bars to the right of the boxplots show the fractional contribution of each air mass type to the total number of air masses in the specific location. The y-values for (c-d) latitude and longitude are the midpoints of the specific coordinate bins.

3.1.2 f(RH) Relationships with Size and Composition

The relative size of particles per air mass can be inferred from the extinction Ångström exponent (AE), which relates the extinction of light at specific wavelengths to particle size (Ångström, 1929), where larger AE suggests smaller particles. Since scattering is the dominant component of extinction, the scattering Ångström exponent (SAE) is often used to relate to particle size. The median SAE values (Fig. 3a) are similar and between 2.09 (MC with Q1 and Q3 of 1.92 and 2.26) to 2.16 (Other with Q1 and Q3 of 1.75 and 2.32) for four of five air masses, indicative of smaller particles. The WP has a median value of 1.37 (with Q1 and Q3 of 1.05 and 1.88), suggestive of the presence of a mixture of accumulation-mode and coarse-mode particles (SAE < 1 occurs for large particles like sea salt and dust) (Schuster et al., 2006; Bergstrom et al., 2007). Past studies have suggested that biomass burning particles exhibit SAE values greater than 1.4, which does not discount the fact that most of the f(RH) data collected during CAMP²Ex is possibly impacted by biomass burning.
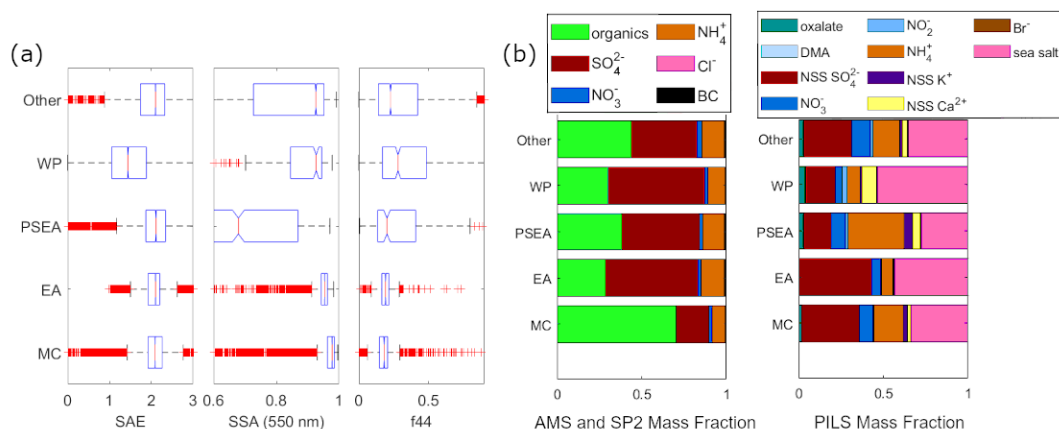
357
358 Figure 3. (a) Boxplots of 1 s scattering Ångström exponent (SAE), single scattering albedo (SSA, 550 nm), and ratio
359 of the mass spectral marker m/z 44 marker relative to total organic mass (f_{44}) and (b) (left) submicron mean organic,
360 SO_4^{2-}, NO_3^-, NH_4^+, Cl^-, and black carbon (BC) mass fractions and (right) bulk (< 5 µm) oxalate, NH_4^+, dimethylamine
361 (DMA), non-sea salt K^+, non-sea salt SO_4^{2-}, non-sea salt Ca^{2+}, NO_3^-, Br^-, NO_2^-, and sea salt mass fractions per air mass
362 (Hilario et al., 2021).

363 One of the indicators of biomass burning in Southeast Asia is organic matter (Adam et al., 2021).
364 The MC air mass (Fig. 3b) has the greatest (71%) mass fraction of organics among the air masses
365 and the highest median SSA (0.98 with Q1 and Q3 of 0.96 and 0.99) (Fig. 3a) that suggests more
366 scattering, rather than absorbing, particles (Moosmüller and Sorensen, 2018). This is consistent
367 with observations from field work in tropical peatland fire in Southeast Asia, where particles were
368 mostly from smoldering combustion and were moderately absorbing, with brown carbon
369 dominating absorbance (Stockwell et al., 2016). Smoldering combustion, which is more common
370 in the Maritime Continent (Reid et al., 2013), is known to produce less elemental carbon (Reid et
371 al., 2005) and potassium (Robinson et al., 2004) compared to flaming combustion. Biomass
372 burning activities were active in the MC during the field campaign (Reid et al., 2023). The MC air
373 mass also has the lowest f_{44} median values (0.18 with Q1 and Q3 of 0.15 and 0.21) (Fig. 3a)
374 suggesting it is the least-oxidized and less photochemically-aged air mass and thus closest to the
375 source compared to other air masses. Chen et al. (2022) who studied tropical peat smoldering
376 (similar to those in MC) showed that primary organics were not oxidized (f_{44} < 0.02) while
377 secondary organics were highly oxidized, that oxidation increases f_{44} (oxidized organics: 0.01 <
378 f_{44} < 0.11), and that high RH speeds up the oxidation process especially for smaller particles (~100
379 nm) (Chen et al., 2022). In the U.S., as another example, f_{44} from wildfire plumes up to 8 hours
380 old did not exceed 0.12 (Garofalo et al., 2019). The high RH during CAMP²Ex (Fig. 1b) likely led
381 to the increased oxidation of secondary organics resulting in median f_{44} values that are relatively
382 high (for all air masses even in MC), suggesting that most of the particles sampled during
383 CAMP²Ex are aged. The high organic mass fraction is consistent with the MC having the lowest
384 median f(RH) as organics are known to reduce aerosol hygroscopicity (Kalberer, 2014; Sorooshian
385 et al., 2017; Shingler et al., 2016a).

386 There is an inverse relationship between hygroscopicity and organic mass fraction data that is most
387 evident in f(RH) values collected within the boundary layer (< 3 km) during CAMP²Ex (Fig. 4a).

388   Those data points that have the highest organic mass fraction values (> 0.6) are also associated
389   with CO concentrations (> 250 ppb) that are typically associated with biomass burning (Shingler
390   et al., 2016a) and are mostly from the MC area (Fig. 4b). The slope of the inverse relationship
391   between f(RH) and organic mass fraction is most steeply negative (-0.81) for the air masses coming
392   from EA (Fig. 4c) .

393
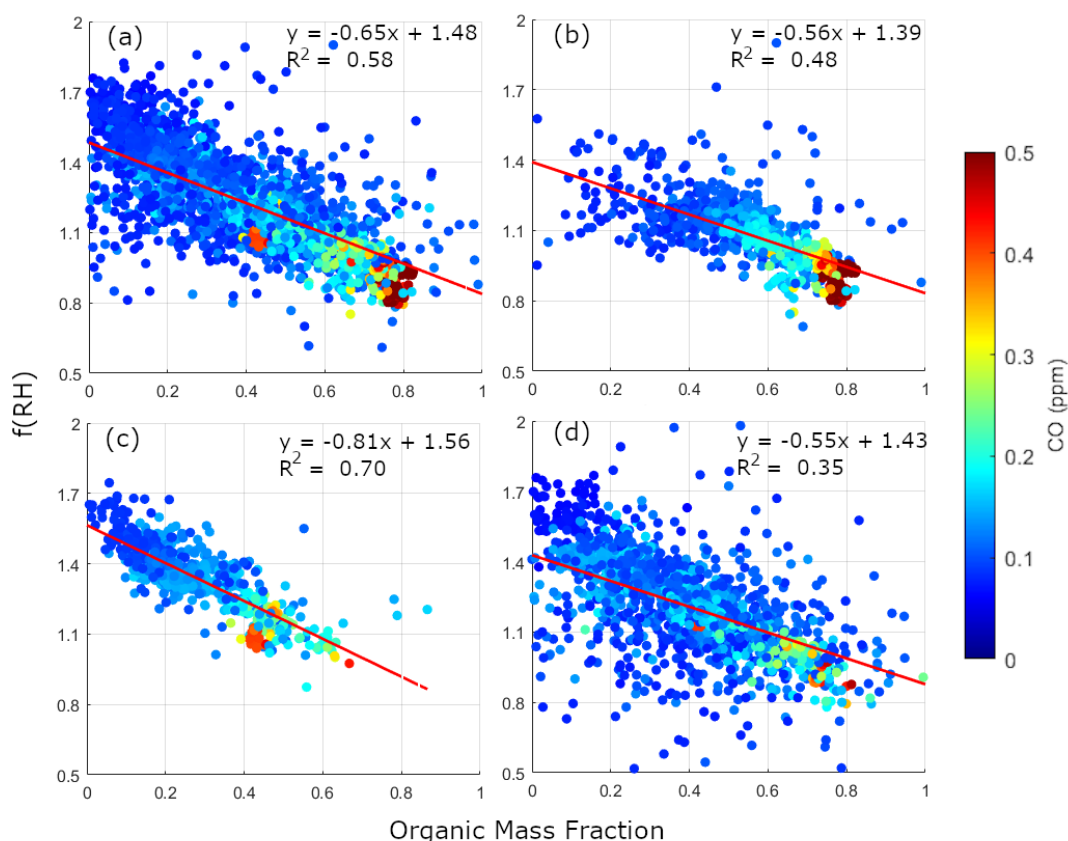
Figure 4. (a-d) Scatter plots of 30 s averaged f(RH) and corresponding organic mass fraction contribution to total
submicron aerosol mass (sum of organic, SO_4^{2-}, NO_3^-, NH_4^+, Cl^-, and black carbon (BC) mass concentration) for (a)
all data collected at altitudes below 3 km and (b-d) for air masses coming from (b) the Maritime Continent (MC), (c)
East Asia, and (d) Other. The dots are colored by their CO concentration.

398   The highest median f(RH) values are from the WP and EA air masses (Fig. 2a). Both have lower
399   organic mass fractions (0.29 and 0.30, respectively), but have distinctly larger aerosol size profiles
400   based on their SAE values (Fig. 3a). The presence of coarser particles from the WP, based on its
401   marine origin (with relatively higher DMA, Fig. 3b) and high sea salt fraction (54%, Fig. 3b),
402   contributed to it having the highest median f(RH) amongst the air masses. The WP air masses
403   appear to have interacted with aged organic particles from biomass burning and industry including
404   fine absorbing particles potentially from industry and dust owing to its relatively high median f_{44}

14

405   (0.26 with Q1 and Q3 of 0.17 and 0.48) and low median SSA (0.93 with Q1 and Q3 of 0.85 and
406   0.95). Particles with predominantly clean marine sources tend to have higher (≥ 0.97) SSA
407   (Dubovik et al., 2002), thus the WP data suggest a polluted marine source (Lacagnina et al., 2015).
408   Though, we note that the air masses from the WP have relatively low scattering and absorption
409   coefficients and that these could have affected the calculations for SSA. EA air exhibits the highest
410   non-sea salt sulfate mass fraction (0.43) (Fig. 3b) that, along with its predominantly fine particle
411   size and median SSA (0.95 with Q1 and Q3 of 0.94 and 0.96), strongly suggests that it was
412   transported from an urban source. Sulfate is a known industrial product of East Asia (Smith et al.,
413   2011; Li et al., 2017; Lorenzo et al., 2023).

414   Particles from PSEA have the lowest median SSA (0.68 with Q1 and Q3 of 0.55 and 0.87) (Fig.
415   3a). This suggests the presence of more absorbing particles relative to scattering, possibly
416   including elemental carbon and aged dust. Based on the PSEA air masses having the highest non-
417   sea salt potassium mass fraction (0.05, Fig. 3b) and highest dust-EC mix among air masses, the
418   particles could be from biomass burning. It is well-documented that dust can be entrained in smoke
419   plumes due to reasons such as turbulent mixing around flames and burn fronts (Palmer, 1981;
420   Kavouras et al., 2012; Maudlin et al., 2015; Schlosser et al., 2017). Dust from East Asia and
421   biomass burning from PSEA have been observed to be mixed in the boreal spring in Taiwan (Dong
422   et al., 2018), and though CAMP^{2}Ex sampled during a different season, it is still possible that this
423   mixing of East Asian dust and PSEA biomass burning could have occurred and impacted the
424   CAMP^{2}Ex region during the field campaign.
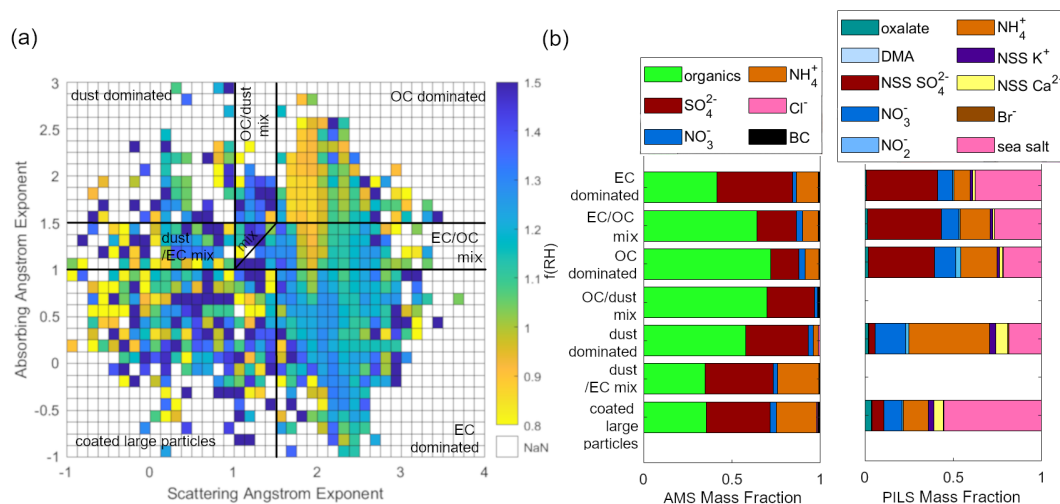
425

426   Figure 5. (a) Median f(RH) of data points with absorbing Ångström Exponent (AAE) and scattering Ångström
427   Exponent (SAE) values that correspond to suggested aerosol types from past studies (Cazorla et al., 2013) with
428   following counts and bulk median f(RH) per aerosol type: EC dominated (16,908 and 1.19), EC/OC mix + mix (20,686
429   and 1.03), OC dominated (1942 and 0.94), OC/dust mix (55 and 1.31), dust dominated (79 and 1.15), dust/EC mix
430   (204 and 1.12), and coated large particles (729 and 1.21). (b) (left) Submicron mean organic, SO_4^{2-}, NO_3^-, NH_4^+, Cl^-,
431   and black carbon (BC) mass fractions and (right) available bulk (< 5 µm) oxalate, NH_4^+, dimethylamine (DMA), non-
432   sea salt K^+, non-sea salt SO_4^{2-}, non-sea salt Ca^{2+}, NO_3^-, Br^-, NO_2^-, and sea salt mass fractions per aerosol type.

433   Using the AAE and SAE with categorization determined by Cazorla et al. (2013), the f(RH) can
434   be related to the types of aerosols. The highest median f(RH) of 1.31 (with Q1 and Q3 of 0.89 and
435   1.46) and 1.21 (with Q1 and Q3 of 0.88 and 1.68) are from the OC/dust mix and coated large
436   particles aerosol types (Fig. 5), respectively, though there are only 55 data points for the OC/dust
437   mix so the aerosol classification for it may not be as robust. As such, there are no PILS
438   compositional data available for the OC/dust mix aerosol type. However, from available data from
439   dust dominated particles, it is also possible that hygroscopic particles like ammonium and nitrate,
440   which have the greatest bulk mass fractions (0.45 and 0.17) in the dust dominated particles
441   compared to other aerosol types, partitioned to dust and increased f(RH) for the OC/dust mix
442   particles. The high f(RH) for the coated large particles is consistent with its the largest bulk sea
443   salt mass fraction (0.56) (Fig. 5b) compared to other aerosol types. Note that the median f(RH)
444   values for the aerosol types may be slightly different than the raw 1 s f(RH) data because the
445   median f(RH) is only calculated for the aerosol types when both the scattering and absorbing
446   Ångström Exponent values are available.

447   Most of the aerosol particles (< 5 µm dry diameter and 93% of all particles) collected during the
448   CAMP^{2}Ex field campaign have optical properties (Fig. 5a) that resembled EC/OC mix + mix (in
449   this case we combined the sub-categories of EC/OC mix and mix) (51%) and EC dominated (42%)
450   aerosol types. The EC dominated particles have the third to the highest median f(RH) at 1.19 (with
451   Q1 and Q3 of 1.05 and 1.33), which is unusual because EC is known to be hydrophobic.
452   Compositional data sheds some light on this, because the particles classified as EC dominated have
453   relatively higher submicron sulfate (0.43) and bulk sea salt mass (0.38) fractions (Fig. 5b)
454   compared to particles classified as OC (0.16 and 0.22) and dust dominated (0.35 and 0.19), which
455   are known to have low hygroscopicity in general. This mixing of sulfate and sea salt with EC
456   dominated particles increases their bulk f(RH). The EC dominated particles come from the EA,
457   MC, and Other air masses. East Asia is a known sulfur source and shipping contributes to sulfate
458   in the region (Miller et al., 2023). Peat smoke particles from MC have also been found in past
459   studies to have sulfate mixed with carbonaceous species (Nakajima et al., 1999). The presence of
460   OC (0.64 submicron mass fraction) decreased the median f(RH) values (Fig. 5b) where the median
461   f(RH) for the EC/OC mix + mix type was 1.03 (with Q1 and Q3 of 0.94 and 1.18).

462   The OC dominated type have the highest submicron organic mass fraction (0.72) and a median
463   f(RH) of 0.94 (with Q1 and Q3 of 0.85 and 1.06), which is consistent with the expected effect of
464   organics to lower hygroscopicity. The median f(RH) values below 1, though, are counterintuitive
465   given that the presence of moisture in the region is thought to generally increase the particle size
466   and consequently the amount of aerosol light scattering. Data where f(RH) is less than unity have
467   been observed in past studies due a number of suspected factors including (but not limited to)
468   volatilization effects, changes in optical properties during humidification, and   particle
469   restructuring (Shingler et al., 2016b).

470

471
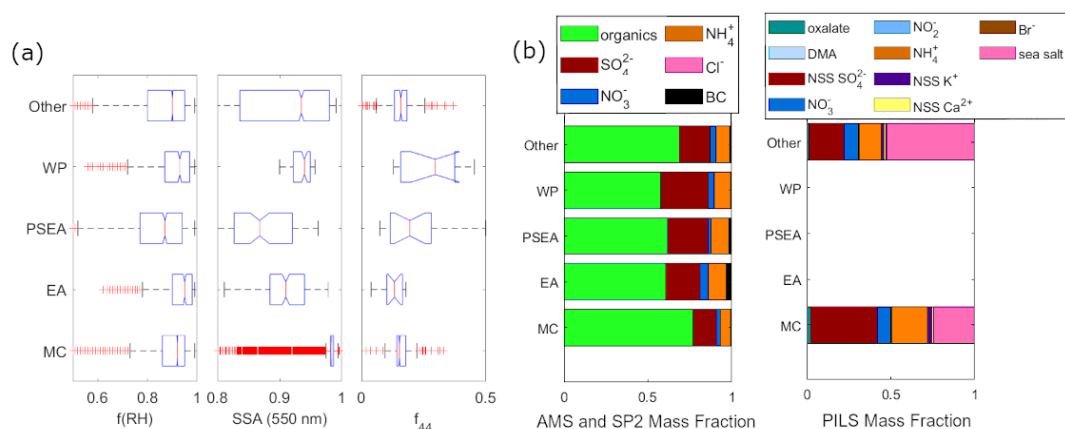
Figure 6. (a) Boxplots of 1 s f(RH) < 1 (MC: 14,612, EA: 473, PSEA: 986, WP: 483, and Other: 9919 counts) and the corresponding single scattering albedo (SSA, 550 nm) and ratio of the mass spectral marker m/z 44 marker relative to total organic mass (f_{44}) and (b) (left) submicron mean organic, SO_4^{2-}, NO_3^-, NH_4^+, Cl^-, and black carbon (BC) mass fractions and (right) available bulk (< 5 µm) oxalate, NH_4^+, DMA, non-sea salt K^+, non-sea salt SO_4^{2-}, non-sea salt Ca^{2+}, NO_3^-, Br^-, NO_2^-, and sea salt mass fractions per regional air mass (Hilario et al., 2021) for times with f(RH) < 1.

To investigate aerosol characteristics when f(RH) is < 1, we plot the f(RH) box plots from each of the regions for data points where f(RH) < 1 (Fig. 6a). There are several instances (26,473 times or 19% of the time for the whole campaign) when the f(RH) was below 1. In general, organic mass fractions greater than 0.75 correspond to sub-1 f(RH) (Fig. 4a). The most prevalent regional air mass association for sub-1 f(RH) is from the MC (f(RH) < 1 from the MC was 56% of all data). The organic mass fraction is dominant (0.57 – 0.77), and almost doubled compared to the whole campaign (Fig. 3b), for all the air masses with sub-1 f(RH) (Fig. 6b) and is highest for the MC (0.77). The organics from the sub-1 f(RH) data are the least aged throughout the campaign for the MC, PSEA, and Other air masses (Fig. 6a). The CAMP²Ex data offer an opportunity to inspect the prevalence of such values and to see what factors coincide with such situations. However, the unique sample make-up of the particles in the CAMP²Ex region makes other reasons, including sample losses due to volatilization, also plausible (Reid et al., 2023). Shingler et al. (Shingler et al., 2016b) also observed such sub-1 values for both f(RH) and the humidified diameter growth factor g(RH) in air masses enriched with carbonaceous components over North America.

The most dominant aerosol types for the sub-1 f(RH) data are the carbonaceous ones (96%) (Fig. 5b), with the EC/OC component contributing the most: EC/OC mix + mix (the combined sub-categories of EC/OC mix and mix) (68%), EC-dominated (18%), and OC-dominated (10%). Both bulk ammonium and sulfate mass fractions for the MC also are higher for the sub-1 f(RH) cases (Fig. 6b) compared to the whole campaign (Fig. 3b, PILS), while the bulk sea salt mass fraction was lower. The bulk sea salt mass fraction of the Other category (Fig. 6b) increases for the sub-1 f(RH). Most of the particles contributing to the sub-1 f(RH) are fine particles (median Ångström Exponent ~2, Fig. 6a) with more reflective characteristics (SSA ≥ 0.90) compared to data for the

17

499 entire campaign. To understand more about sub-1 f(RH), we will look at a selected case in the
500 succeeding section.

3.2   Case Studies

3.2.1 Sub-1 f(RH) from Biomass Burning Smoke

503 The chosen case study is part of a flight on 16 September 2019 that occurred closest to the Maritime
504 Continent, which is the source of the air masses that had the most counts of sub-1 f(RH) (Section
505 3.1.2). This flight coincided with an active biomass burning event on 14 September 2019 (NASA,
506 2020) and fire hotspots in the Maritime Continent were numerous throughout September 2019
507 (Othman et al., 2022). The back trajectories at 01:00 UTC, when the aircraft began to make
508 measurements closest to the surface (~300 m altitude) and perpendicular to the wind, all come
509 from the southwest of the aircraft location (Fig. 7a), in the direction from where biomass burning
510 emissions were being transported. Details about the flight and conditions during this case study
511 are found in Crosbie et al. (2022). In their study they note the smoke to be from Kalimantan with
512 an age between 48 and 72 h. Consistently low f(RH) (all below 1, Fig. 7b) values were observed
513 for a little less than an hour, until the aircraft began its ascent (Fig.7b). The aerosol mass
514 concentrations of >70 µg m^{-3} were among the highest in the entire field campaign and were
515 dominated by organics (Fig. 7b).
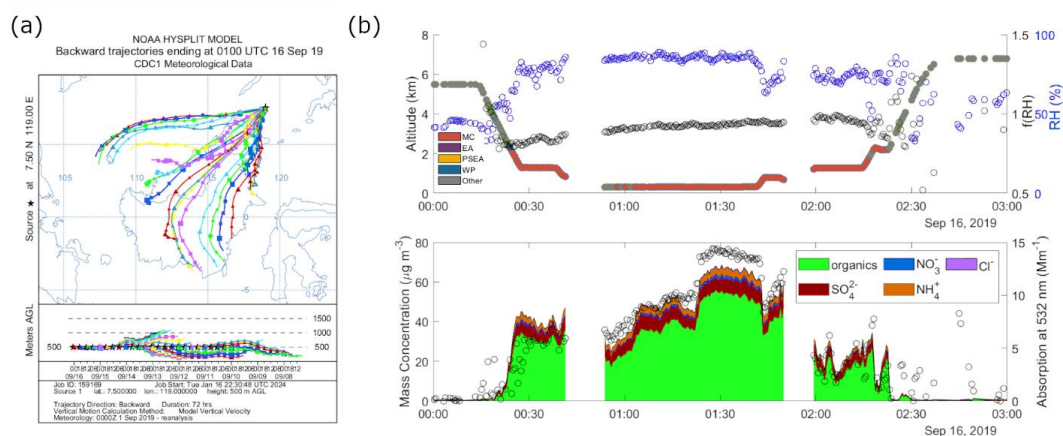
516

517 Figure 7. Case study of sub-1 f(RH) on 16 September 2019. (a) Five-day back trajectories at the approximate flight
518 location at 01:00 UTC. (b) (top) Time series plots of altitude colored by regional air mass, f(RH) in black circles, and
519 RH (blue circles), and (bottom) aerosol mass concentrations from the AMS and absorption at 532 nm (black circles)
520 during one of the flight legs closest to the surface from 00:00 to 03:00 UTC.

521 The sub-1 f(RH) during the lowest altitudes of the aircraft, from 01:00 to 01:40 UTC, are correlated
522 with approximations of the submicron particle effective density (Fig. 8a). Absorption
523 measurements along with back trajectories linked to active fires point to the increasing presence
524 of EC and brown carbon with increasing particle density (even if there were no valid EC

18

525 measurements for this specific time). Submicron number concentration, dry absorption (532 nm),
526 organic mass fraction, and single scattering albedo are highest for the smallest effective density
527 values for sub-1 f(RH) (Fig. 8b) during the entire campaign, likely due to the presence of EC and
528 OC. This is consistent with the most dominant aerosol type during the field campaign, which is a
529 mix of elemental and organic carbon based on SAE and AAE values. The dataset cannot be used
530 to prove particle restructuring and very likely the sub-1 f(RH) values are due to other factors since
531 particles' history included passes through humid areas where restructuring presumably would have
532 already occurred prior to reaching the aircraft. In addition, smoldering from peat, which is
533 dominant in the MC fires (Reid et al., 2023), is known to produce homogenous spheres with no
534 voids and similar to OC (Pokhrel et al., 2021), making restructuring unlikely to be the dominant
535 mechanism to explain our findings. However, we present these results for the sake of documenting
536 a Southeast Asia case of these unusual events occurring in EC/organic-rich air masses similar to
537 past work (e.g., Shingler et al., 2016b and references therein) to emphasize that these events occur
538 throughout the world and to motivate more research into the matter.
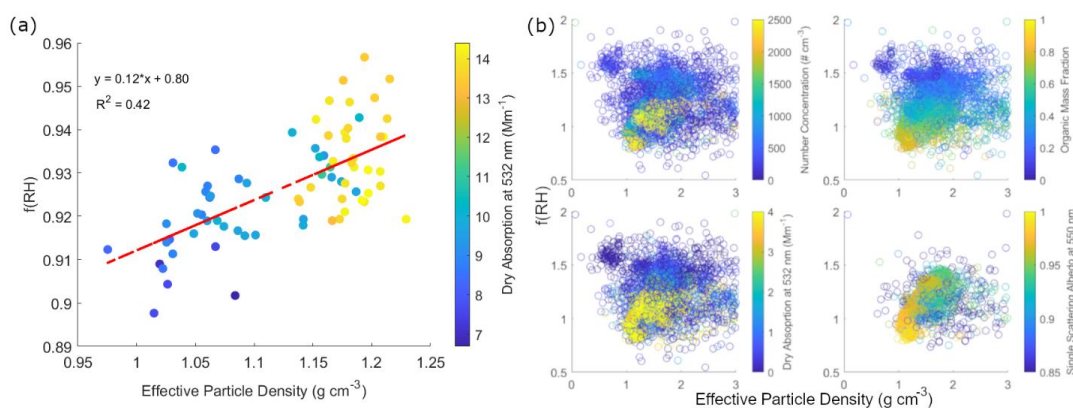
540 Figure 8. 30 s f(RH) and effective particle density plots for (a) 16 September 2019 from 01:00 to 01:40 UTC colored
541 by dry absorption at 532 nm, and (b) for the entire CAMP²Ex field campaign and colored by (clockwise from top left)
542 LAS number concentration of particles with diameters between 100 and 1000 nm, organic mass fraction, single
543 scattering albedo at 550 nm, and dry absorption at 532 nm.

544 Smoke particles are known to have a range of density values, depending on their degree of
545 atmospheric aging, affecting their size, and the processes they undergo. The effective particle
546 density is usually lower for biomass burning particles from smoldering that have larger diameters
547 (Pokhrel et al., 2021), compared to flaming. Freshly emitted smoldering particles have effective
548 densities from 1.03 g cm⁻³ to 1.21 g cm⁻³ that do not vary much with diameter based on a laboratory
549 study (Pokhrel et al., 2021). Our calculated values fall within this range (Fig. 8). This adds
550 confidence to our observation that organics (brown carbon), which dominate smoldering
551 emissions, are the major contributors to the sub-1 f(RH). Both aerosol hygroscopicity and effective
552 particle density are important for properly modeling cloud condensation nuclei, one of the most
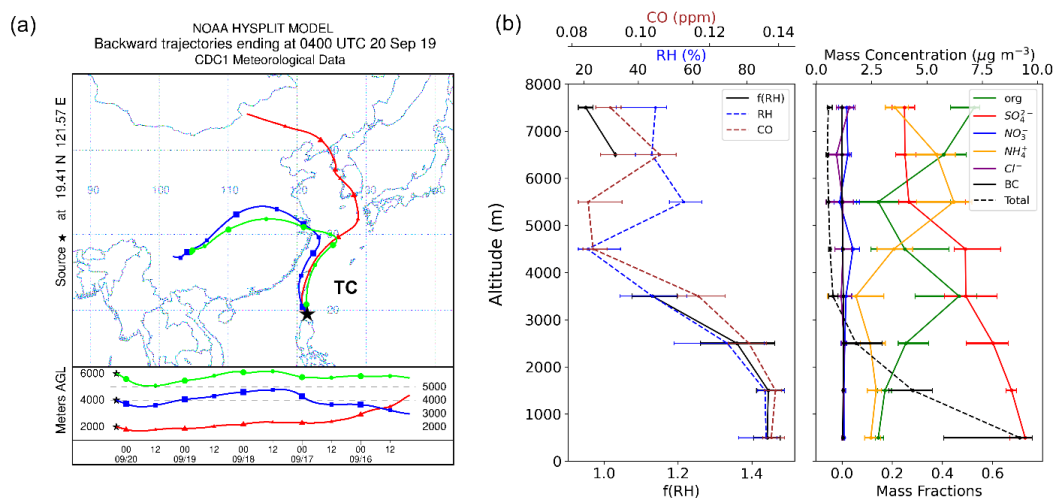553 important factors in aerosol-cloud interactions.

19

3.2.2 Vertical Transport

The vertical distribution of aerosols affects cloud formation, we investigate this through two cases of aerosol vertical transport. The vertical transport cases were identified from averages of the available vertical profiles made during CAMP²Ex. A large-scale event (01:53 to 06:20 UTC 20 Sep 2019) north of Luzon, Philippines, due to a tropical cyclone, and a smaller-scale event (02:55 to 06:02 UTC 24 Sep 2019) east of Luzon, due to shallow convection were chosen for the case studies. The measured median CO mixing ratio was used as a tracer for vertical transport (Kar et al., 2004). An increase in the median CO mixing ratio at higher altitudes along with multi-level winds from a similar direction were the main criteria used to identify the cases.

Northerly to northwesterly winds are the dominant source for the first case (Fig. 9a) influenced by tropical cyclone Tapah (TC Tapah's center was ~600 km northeast of the aircraft location). This suggests the influence of East Asia on the sample as described in Crosbie et al. (2022), where the meteorology is discussed in more detail. There is a general decrease in f(RH) from the lower levels that follows a similar trend to the decrease in total mass (Fig. 9b) and sulfate mass fraction. Sulfate is hygroscopic so it is understandable that the f(RH) decreased with altitude as the sulfate decreased. The increase in CO between 6-7 km (Fig. 9b) suggests vertical transport aloft and was accompanied by a subsequent decrease in f(RH) and an increase in organic mass fraction (Fig. 9b) between 6-8 km. This is consistent with analysis in the previous sections, which show decreased f(RH) with increased organic mass fractions.

Accompanying the general decrease of f(RH) with altitude are decreasing submicron median volume size distribution (VSD) magnitudes and volume weighted average diameters (Fig. 10). Possible reasons for these trends are that larger hygroscopic particles, such as sulfate (which make up the largest mass fraction at lower levels), were scavenged (especially at lower altitudes) and/or activated into cloud drops, leaving the smaller particles behind. Submicron aerosol mass also decreases with altitude, with values below 1 μg m^{-3} (Fig. 9b). There is a slight increase in VSD from 6-8 km compared to 4-6 km, and especially at larger diameters, broadening the VSD curve which may suggest cloud processing (Eck et al., 2012). Though sulfate enhancements have traditionally been the marker for cloud processes (Barth et al., 2000; Faloona, 2009), more recent studies have observed potential cloud processing cases with increased organics (i.e. Wonaschuetz et al., 2012; Dadashazar et al., 2022). This case could thus be showing vertically transported organic matter that has possibly affected or was affected by the clouds between 6-7 km. Another observation is the increase of ammonium and nitrate mass fractions above 4 km (Fig. 9b). There is no corresponding valid f(RH) data, and we can only infer based on the CO profile that begins to shift toward a more positive slope with increasing altitude that this increase in ammonium could also be associated with cloud processing. Ammonia is abundant in East Asia (Pawar et al., 2021) And although there are still limited studies, the scavenging efficiencies of organics and ammonium (compared to sulfate) could also be contributing to their increasing mass fractions with altitude (Yang et al., 2015; Hilario et al., 2023).

Figure 9. Case study of tropical cyclone-induced convection on 20 September 2019. (a) Five-day multi-level back trajectories from the average location of the aircraft from 01:53 to 06:20 UTC with the approximate TC center location and (b) vertical profiles (median, 25 and 75th percentiles) of (left) f(RH), relative humidity (RH), and CO mixing ratio and (right) submicron mass fractions of organics, sulfate, nitrate, ammonium, and black carbon and sum of mass concentrations from AMS and SP2 (dashed black line) for 1 km altitude bins.
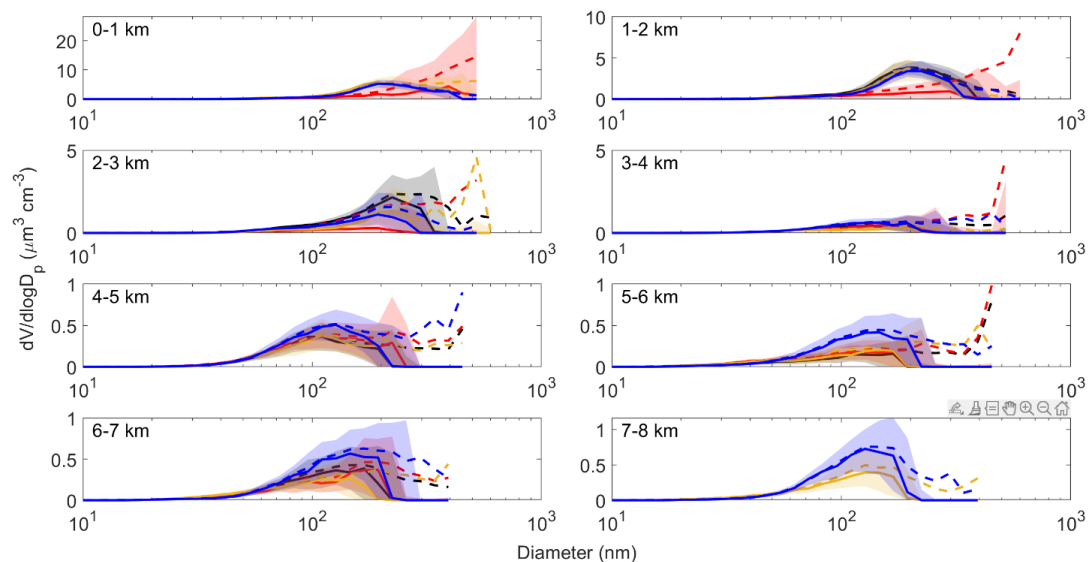
Figure 10. Median (solid line), mean (dashed line), and 25th to 75th percentiles (shaded area) of volume size distributions of submicron particles (FIMS) every 1 km altitude for the case study of tropical cyclone-induced convection on 20 September 2019 from 01:53 to 06:20 UTC. The colors represent four separate vertical profiles, where black was from 01:35 to 02:19 UTC, red was from 03:40 to 04:44 UTC, yellow was from 04:59 to 05:27 UTC, and blue was from 05:52 to 06:20 UTC.

21

604 The second case, the shallow cumulus case on 24 September 2019 (Hilario et al., 2023), has multi-
605 level wind trajectories initially from the West Pacific in the northeast direction, which appear to
606 have come from the Philippines and the general southwest direction from two days before (Fig.
607 11a). The most evident increase in CO (Fig. 11b) is observed between 5-5.5 km, at an altitude
608 lower than the previous case. Both RH and f(RH) have a similar trend to CO throughout the vertical
609 profile, which slightly follows the trend of sulfate mass fraction. This is observed especially in the
610 lower levels (until ~2 km) where RH and f(RH) are relatively steady, even with a large decrease
611 in total aerosol mass.

612 At higher altitudes, above 4.5 km, f(RH) increases to a greater degree with decreased organic mass
613 fraction and increased sulfate mass fraction (Fig. 11b), possibly due to cloud processing. Like the
614 first case, the VSD plots (Fig. 12) for this case show decreasing VSD magnitudes and volume
615 weighted average diameters with increasing altitudes. The broadening of the VSDs above 3 km,
616 concurrent with the increased decreased sulfate mass fraction, likewise suggests cloud processing.
617 There is a known sulfate source, a power plant in western Luzon, in the Philippines that is along
618 the path of the l.5 km back trajectory (Fig. 11a) and may possibly contribute to sulfate in the region
619 (Lorenzo et al., 2023). It is possible that this and other sulfate sources in the region, such as those
620 from ships (Miller et al., 2023), are being transported vertically and affecting aerosol
621 hygroscopicity in the areas where there is shallow convection.
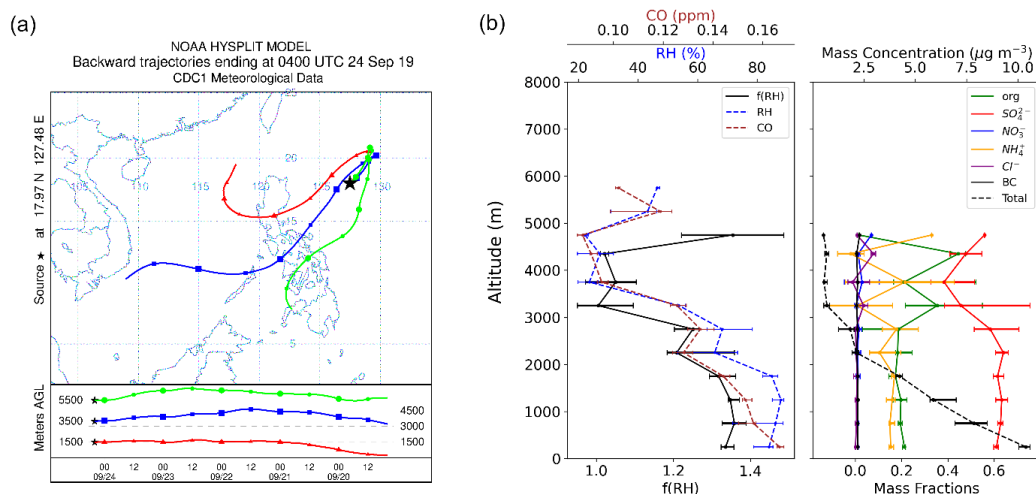
622

623 Figure 11. Case study of shallow convection on 24 September 2019. (a) Five-day multi-level back trajectories from
624 the average location of the aircraft from 02:55 to 06:02 UTC and (b) vertical profiles (median, 25 and 75th percentiles)
625 of (left) f(RH), relative humidity (RH), and CO mixing ratio and (right) submicron mass fractions of organics, sulfate,
626 nitrate, ammonium, and black carbon and sum of mass concentrations from AMS and SP2 for 0.5 km altitude bins.

22
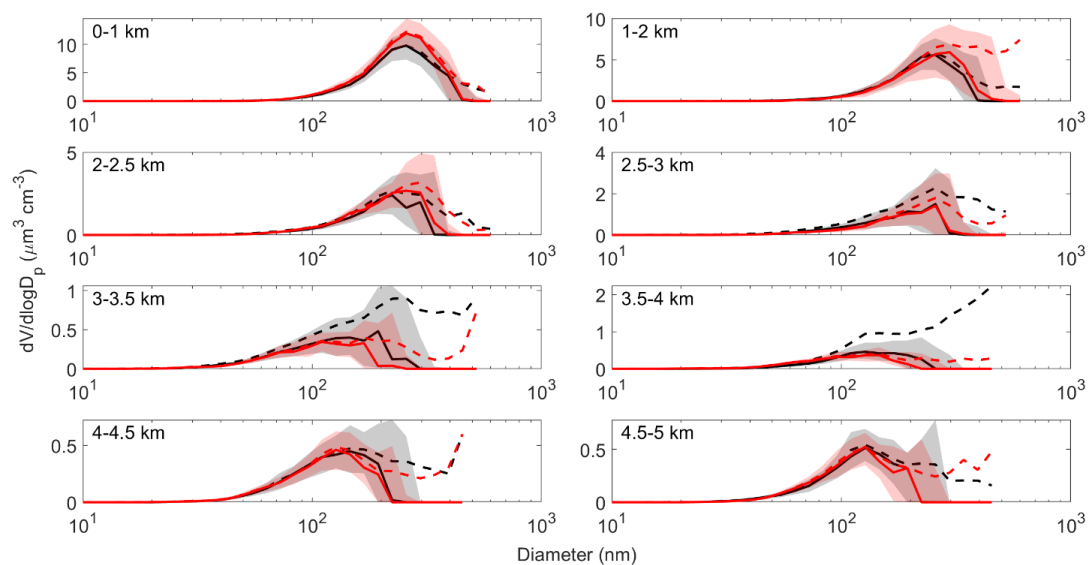
Figure 12. Median (solid line), mean (dashed line), and 25th to 75th percentiles (shaded area) of volume size distributions of submicron particles (FIMS) in 0.5-1 km altitude increments for the case study of shallow convection on 24 September 2019 from 02:55 to 06:02 UTC. The colors represent two separate vertical profiles, where black was from 02:55 to 04:07 UTC and red was from 05:42 to 06:02 UTC

In summary, for both cases vertical transport in cumulus clouds results in higher f(RH), lower sulfate mass fraction, and higher organic mass fraction at cloud outflow altitudes. The VSDs and the averaged diameter of the aerosol size decrease from cloud base to cloud outflow altitudes, likely due to cloud processing. The understanding and representation of the vertical transport or aerosols due to the tropical cyclone and shallow convection and their role in aerosol-cloud interaction is further investigated as we evaluate modeled data using the two cases that we have just discussed.

3.2.3 Model Evaluation

To give regional context to the cases, we begin the discussion of model evaluation with the horizontal distribution of the modeled (~111 km resolution) near-surface aerosol hygroscopicity (kappa: calculated from the volume fractions and kappa values (Eq. 3) of the modeled submicron aerosol species as described in 2.3.2) and winds within the CAMP^{2}Ex domain. We will compare the model kappa values to kappa from different regions around the world based on previous studies. Subsequently, we will discuss how the modeled kappa at different vertical levels compare to the kappa derived from bulk f(RH) (< 5 µm) (Eqs. 4 and 5) as well as from kappa derived from submicron AMS and SP2 species (Eq. 3) from the aircraft observations.

The CAM-chem modeled surface kappa values (Fig. 13) in the CAMP^{2}Ex region of interest, during the time when the three cases discussed in 3.2.1 and 3.2.2 were sampled, are within the range of globally modeled surface kappa in marine (0.9 – 1.0), continental (0.1 – 0.4), and continental

23

651   outflow (0.4 – 0.6) regions from previous studies (Pringle et al., 2010). The highest modeled kappa
652   (~1.0, Figs. 13a and 13b) is like those previously found in marine areas and is influenced by the
653   high winds, coming from the direction of the Pacific Ocean, and can increase sea salt emissions.
654   This is due to the tropical cyclone which was still developing on 16 September 2019 and more
655   fully developed on 20 September 2019. The Pacific Ocean also is the source of high kappa (~0.9
656   - 1.0) for the shallow convection case on 24 September 2019 (Fig. 13c). For all three cases there
657   was low kappa (< 0.4) in areas with low wind speeds and over land especially over Borneo and
658   East Asia, typical of continental and continental outflow regions. For the two cases that were
659   within the southwest monsoon (Figs. 13a and 13b) the lowest kappa values (< 0.2) were in Borneo
660   and downwind areas including Southern Philippines and areas east of it.

661   The modeled surface kappa (~0.1 – 0.5) below the aircraft positions for the case studies of interest
662   (red lines in Fig. 13), though over the sea, are lower than in those areas most affected by the Pacific
663   Ocean and are influenced by emissions from Borneo (Figs. 7a and 13a), East Asia (Figs. 9a and
664   13b) and the Philippines (Fig. 11a and 13c) based on back trajectories. Kappa, calculated from the
665   median f(RH) derived from scattering measurements, for the five air masses discussed in sections
666   3.1 and 3.2 (MC: -0.02, EA: 0.14, PSEA: 0.10, WP: 0.24, and Other: 0.11), all fall in the
667   continental category even though the majority of these air masses are technically in regions with
668   continental outflow. The CAM-chem kappa values for the maritime continent are very close to
669   zero, but in the aircraft positions for the case studies with vertical transport (Figs. 13b and 13c) the
670   CAM-chem kappa values (~0.40 – 0.50) are more than double the range of calculated kappa from
671   East Asia (0.14) and Other (0.11) air masses that are influencing the case studies. To make sense
672   of this difference between globally modeled surface kappa values and that which is calculated from
673   the CAMP²Ex f(RH), we delve more into aerosol vertical transport and its connection to aerosol
674   hygroscopicity and evaluate the vertical profile of the kappa calculated from the CAM-chem model
675   outputs.
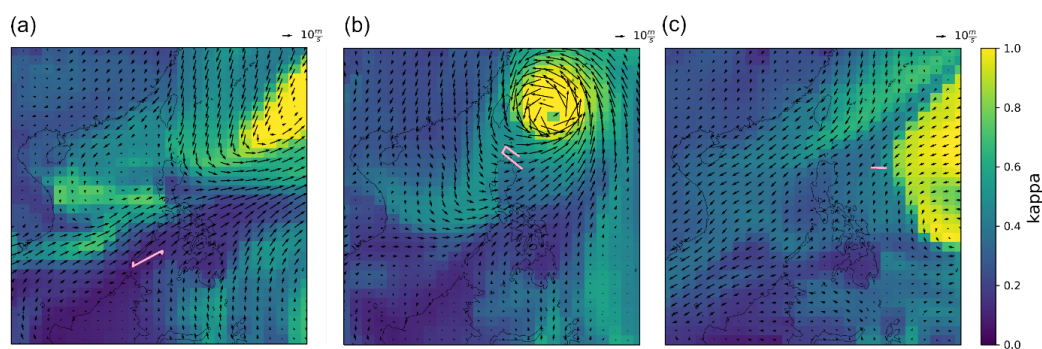
676

677   Fig. 13. Modeled kappa and winds at 957 hPa for (a) the biomass burning smoke case at 06:00 UTC on 16 September
678   2019, (b) the tropical cyclone-induced case at 06:00 UTC on 20 September 2019 and, (c) the shallow convection case
679   at 06:00 UTC on 24 September 2019. The pink lines represent the aircraft locations from 02:15 to 04:22 UTC on 16
680   September 2019, 01:53 to 06:20 UTC on 20 September 2019 and, from 02:55 to 06:02 UTC on 24 September 2019.

681   The CAM-chem model (Fig. 14a) was able to represent the general trends in the observed total
682   submicron mass vertical profile for the tropical cyclone-induced convection case. The observations
683   from AMS are only for non-refractory aerosol species, however, and so sea salt and dust are not
684   included in the total mass, possibly affecting the comparison with the model output, which
685   accounts for both. The uniform ~111 km grid mesh CAM-chem and MUSICA outputs show
686   approximate contributions by sea salt and dust to be 5 to 20% of the total mass (Figs. 15b and 15c).
687   This could explain the relatively higher total mass values from the model outputs compared to
688   observations for some altitude levels, though in general even without dust and sea salt the CAM-
689   chem model still has slightly higher aerosol total mass values (dashed lines in Fig. 14a) compared
690   to the observations. The CAM-chem model represents the approximate aerosol total mass well for
691   this case probably because of its large-scale nature, where wind speeds were relatively high and
692   where the aerosol particles are potentially from a large source (East Asia) (Figs. 9a and 13a).
693   Together, the sum of the sulfate and ammonium mass fractions are similar for the observed (Fig.
694   15a) and modeled outputs close to the surface (Figs. 15b and 15c), where the model output is
695   ammonium bisulfate and not just sulfate, and the actual mass concentrations of the models are
696   generally higher than the observations above 1 km (Fig. S1a). This sulfate-based compound
697   dominates the total aerosol mass for both the observations and model outputs, as is expected based
698   on its source air mass from East Asia, and accounts for the similar observed and modeled total
699   mass shape profiles (Fig. S1). The organic mass fraction, on the other hand, is lower by almost
700   half of the observed organic mass fraction due to sulfate dominating. This has a direct effect on
701   modeled aerosol hygroscopicity (kappa), as it has been shown earlier that f(RH) decreases with
702   increased organic mass fraction (Fig. 4).

703
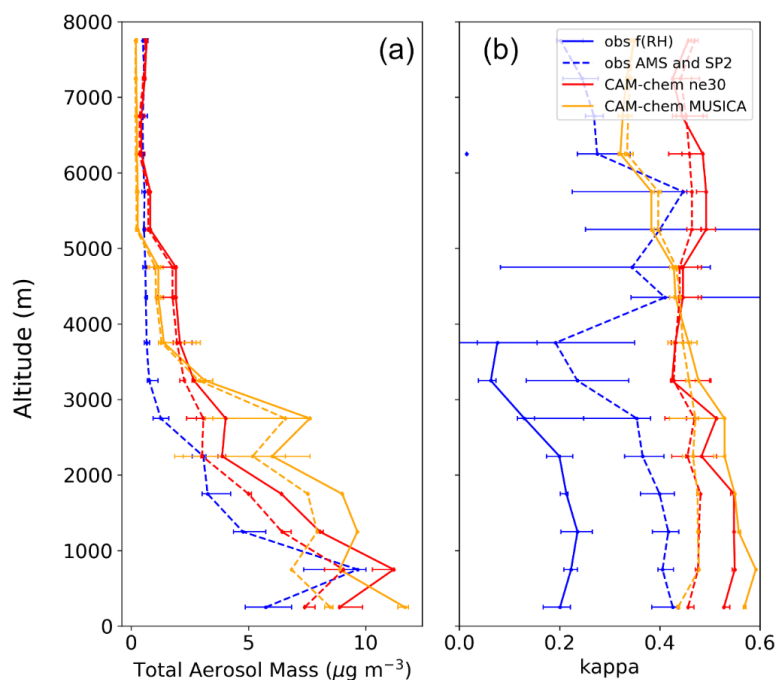
Figure 14. Vertical profiles of observed data (01:53 to 06:20 UTC) and CAM-chem model outputs (06:00 UTC) for ne30 ~1° and MUSICA 0.25° grids for the tropical cyclone-induced convection case on 20 September 2019 at 500 m intervals. (a) Total observed submicron aerosol mass from AMS (organics, SO_4^{2-}, NO_3^-, NH_4^+, Cl^-) and SP2 (black carbon (BC)) data and CAM-chem output (organics: primary/hydrophobic, hygroscopic, and secondary ($C_{15}H_{38}O_2$), sulfate (NH_4HSO_4), sea salt, dust ($AlSiO_5$), and black carbon (primary/hydrophobic and hygroscopic)) where the solid line includes all the CAM-chem species and the dashed line excludes dust and sea salt and (b) calculated kappa from observed f(RH) (solid line, < 5 µm) and from AMS and SP2 (dashed line, submicron) data and using ZSR mixing rule for all CAM-chem aerosol species (solid line, submicron) and excluding dust and sea salt (dashed line). The lines correspond to the median values of data in the given altitude intervals and the bars correspond to the 25th and 75th percentile values.

Median modeled kappa for the tropical cyclone-induced convection case is more than twice in magnitude compared to the median derived kappa from f(RH) (Fig. 14b), though they have a similar vertical profile shape. It has been noted from previous studies that the conversion of observed f(RH) to kappa may be associated with up to 40% uncertainty (van Diedenhoven et al., 2022), though this does not change that the kappa from CAM-chem is still approximately twice the calculated observed kappa. Kappa calculated from f(RH) represents larger particles (< 5 µm) compared to the kappa calculated from CAM-chem (< 0.48 µm), and the difference in size of the particles could be contributing to this disparity in kappa.

We compare more similar sized particles, kappa derived from AMS and SP2 measurements (< 0.70 µm) with kappa calculated from CAM-chem (Fig. 14b) and find that the kappa derived from the AMS and SP2 is still lower than that computed from CAM-chem outputs. The kappa from

26

725   AMS and SP2 is approximately twice (100% larger than) the kappa from f(RH), probably due to
726   particle size differences. Based on Mie theory and studies comparing f(RH) of PM_1 and PM_{10}
727   particles (Zieger et al., 2013; Titos et al., 2021), $CAMP^2Ex$ f(RH) would be larger if it were
728   measuring just submicron particles due to the increased scattering efficiency for accumulation
729   mode particles compared to coarse particles. Though, based on Fig. 3 of Titos et al. (2021), the
730   difference in f(RH) in marine sites would only be ~0.1 (given median observed SAE) and that
731   would translate to ~20 to 40% increase in kappa. Thus, although size plays a role, composition is
732   also contributing to the difference in the calculated kappa values between observations and the
733   model.

734   The over and under-represented mass of sulfates and organics, respectively (Fig. 14b), by the
735   model may be causing the higher kappa in the model. Based on the discussion in section 3.1.2 on
736   air masses coming from East Asia (Fig. 4c), as is the case for this event, an organic mass fraction
737   that is lower by half can increase the f(RH) (f(RH) = (-0.81 * organic mass fraction) + 1.56) and
738   therefore the derived kappa by ~70%. Organics, especially secondary organic aerosols have been
739   underpredicted by CAM-chem in urban and urban outflow regions (Schwantes et al., 2022). This
740   is consistent with the observations for this case, which is influenced by urban outflow from East
741   Asia and thus affecting the calculated kappa from the model.
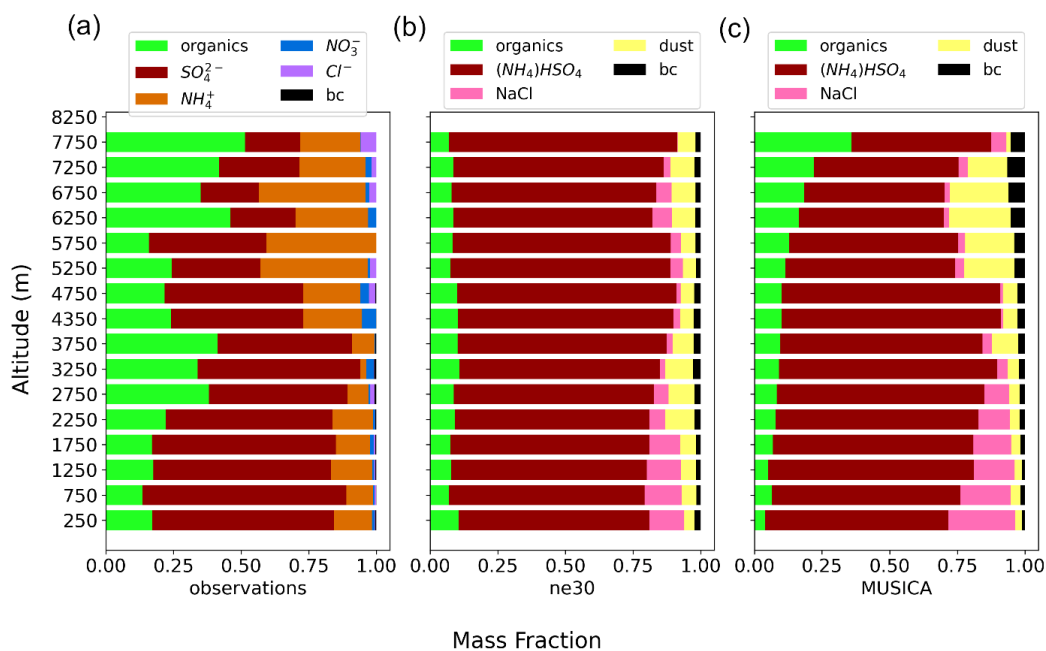

742

743   Figure 15. Vertical profiles of submicron median mass fractions at 500 m intervals of (a) observational data (01:53 to
744   06:20 UTC) and (b-c) corresponding CAM-chem model outputs (06:00 UTC) for (b) ne30 ~1° and (c) MUSICA 0.25°
745   grids for the tropical cyclone-induced convection case on 20 September 2019. CAM-chem outputs were combined
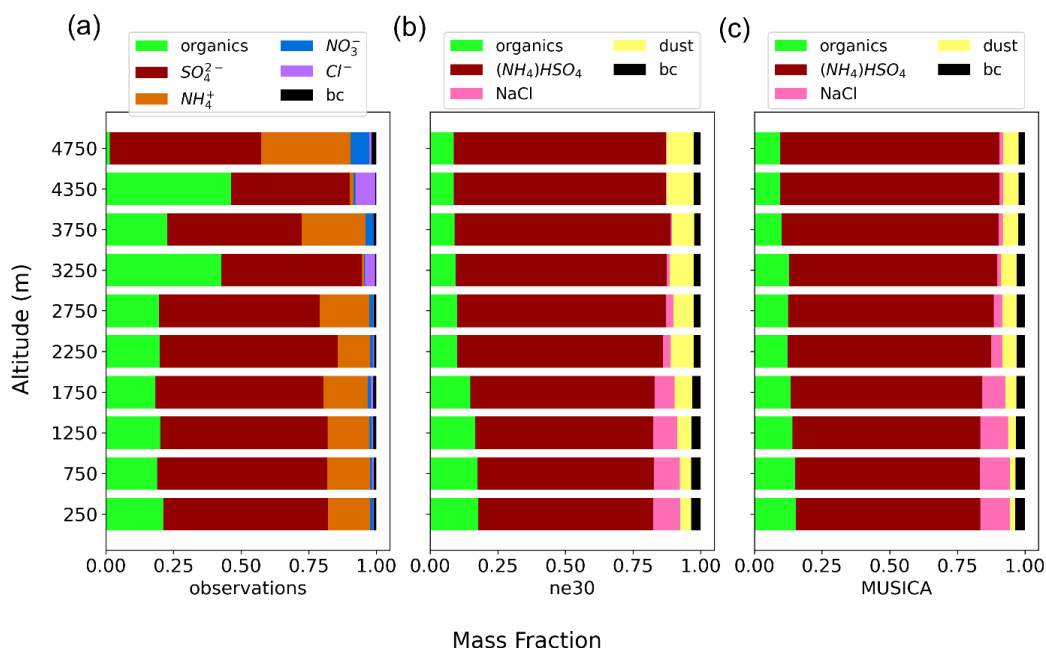
27

746   into five main categories: organics (primary/hydrophobic, hygroscopic, and secondary ($C_{15}H_{38}O_2$)); sulfate
747   (NH_4HSO_4); sea salt; dust ($AlSiO_5$); and black carbon (primary/hydrophobic and hygroscopic).

748   For the case of shallow convection, the shape of the vertical profile of the CAM-chem model
749   output total mass concentration is similar to the observed total mass concentration profile (Fig.
750   16a), though it underestimates the observed total concentration by approximately 2 to 4.5 µg m^{-3}
751   below 1 km altitude, and then overestimates concentrations by approximately 0.5 to 2 µg m^{-3} above
752   1 km. This is due to the model underestimating organics and sulfate close to the surface, while
753   sulfate is overestimated above 1 km (Fig. S1b). The effect of this is seen in the model-derived
754   kappa, which is, like the previous case, higher than the calculated kappa from observations, though
755   to a lesser degree (Fig. 16b). Unlike the case of the tropical cyclone-induced convection, the
756   modeled kappa is relatively unchanging in shape compared to the kappa derived from
757   observations. This is likely due to the differences in the compositional profile at the higher
758   altitudes, even if the total mass is similar. The model is not able to represent the increase and
759   decrease in organic mass fraction from 3.5 to 4.5 km (Fig. 17a) and dominance of sulfate above
760   4.5 km. At those altitudes the observations become dominated by sulfate, ammonium, and nitrate
761   (Fig. 17a), even with losses due to scavenging and activation as shown by decreased aerosol mass
762   with altitude, probably due to the in-cloud production of sulfate as discussed in section 3.2.2. The
763   mass fraction profiles from the model (Fig. 17b) appear to have a steadily decreasing (increasing)
764   organic and sea salt (sulfate and dust) mass fraction with height. This case is a smaller scale event
765   with smaller surface winds associated with it (Fig. 13b) compared to the tropical cyclone case.
766   With weak forcing, it is likely that the CAM cumulus parameterizations does not predict the
767   convection observed in the shallow convection case affecting modeled aerosol mass vertical
768   distribution and, consequently, kappa in both the uniform ~111 global model and the regionally
769   refined simulations. This is similar to another model evaluation study (i.e. GEOS and GOCART)
770   for the CAMP[2]Ex data, which recommended an improvement of shallow convection schemes to
771   improve the representation of vertical transport (Collow et al., 2022). In fact, the CO increase
772   above 5 km, that that we used to identify convection, is not captured by CAM-chem (Fig. S2).
773   What is consistent though is that for both the observations and model output of this shallow
774   convection case, the relative magnitude of the model kappa is lower than that of the tropical
775   cyclone case.

776
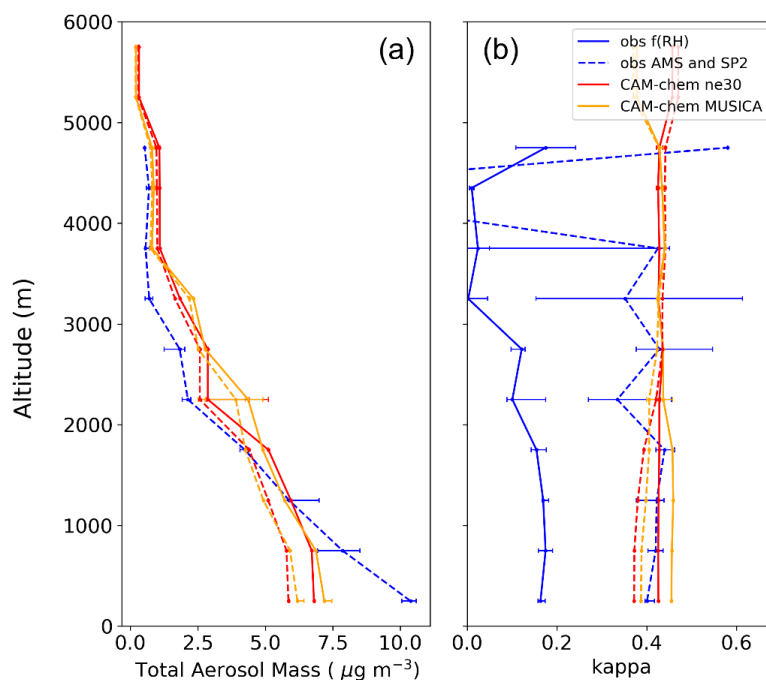
Figure 16. Vertical profiles of observed data (02:55 to 06:02 UTC) and CAM-chem model outputs (06:00 UTC) for ne30 ~1° and MUSICA 0.25° grids for the shallow convection case on 24 September 2019. (a) Total observed submicron aerosol mass from AMS (organics, SO_4^{2-}, NO_3^-, NH_4^+, Cl^-) and SP2 (black carbon (BC)) data and CAM-chem output (organics: primary/hydrophobic, hygroscopic, and secondary ($C_{15}H_{38}O_2$), sulfate (NH_4HSO_4), sea salt, dust ($AlSiO_5$), and black carbon (primary/hydrophobic and hygroscopic)) where the solid line includes all the CAM-chem species and the dashed line excludes dust and sea salt and (b) calculated kappa from observed f(RH)) (solid line) and from AMS and SP2 (dashed line) data and using ZSR mixing rule for all CAM-chem aerosol species (solid line) and excluding dust and sea salt (dashed line). The lines correspond to the median values of data in the given altitude intervals and the bars correspond to the 25th and 75th percentile values.

Figure 17. Vertical profiles of submicron mass fractions at 500 m intervals of (a) observational data (02:55 to 06:02 UTC) and (b-c) corresponding CAM-chem model outputs (06:00 UTC) for (b) ne30 ~1° and (c) MUSICA 0.25° grids for the shallow convection case on 24 September 2019. CAM-chem outputs were combined into five main categories: organics (primary/hydrophobic, hygroscopic, and secondary ($C_{15}H_{38}O_2$)); sulfate (NH_4HSO_4); sea salt; dust ($AlSiO_5$); and black carbon (primary/hydrophobic and hygroscopic).

4. Conclusion

This study reports on low PM_5 ($D_p < 5$ μm) aerosol hygroscopicity measured during CAMP[2]Ex 2019 in Southeast Asia due to organics from biomass burning. Aging and vertical transport changes the hygroscopicity of particles affecting clouds and cloud representation in models in the region, emphasizing the need to improve emissions inventories and shallow cloud parameterizations. Notable results of this work, following the study goals raised at the end of Section 1 are as follows:

The generally low median f(RH) (1.24 with Q1 and Q3 of 1.05 and 1.43) of aerosol particles (< 5 μm) in Southeast Asia during the CAMP[2]Ex campaign from 24 August to 5 October in 2019 is linked to the dominating regional effect of biomass burning from the Maritime Continent. The median f(RH) of air masses from the Maritime Continent was exceptionally low (1.05 with Q1 and Q3 of 0.94 and 1.20). Measurements of f(RH) in other polluted marine environments around the world for PM_{10} (< 10 μm) and PM_1 (< 1 μm) particles have higher ranges (median of ~1.7 – 2.0) of f(RH) values (Titos et al., 2021). The air masses with the highest f(RH) from CAMP[2]Ex are generally from the West Pacific, in the northernmost regions of the Philippines and farthest

807   away from the Maritime Continent. Their median f(RH) (1.49 with Q1 and Q3 of 1.26 and 1.73)
808   is also lower than what has been associated with typical polluted marine environments.

809   Throughout CAMP^{2}Ex, submicron organic matter is the main aerosol component associated with
810   biomass burning and the low f(RH) values. Organics are a major feature of total aerosol mass,
811   especially in air masses traced back to the Maritime Continent. Biomass burning smoke is spread
812   out in the region contributing to elevated AOD downwind of the MC (Fig. 2 in Reid et al. (2023))
813   and is corroborated by cases of sub-1 f(RH) and submicron reflective particles with high organic
814   mass fractions that are present in all the air masses. Based on clustering analysis using optical
815   properties, majority of the particles sampled during the campaign appear to be a mixture of both
816   elemental and organic carbon. Organics dominate in terms of mass fraction due to the smoldering-
817   type burning in peat fire (Reid et al., 2023) from the Maritime Continent, which is known to
818   produce more organics than elemental carbon (Reid et al., 2005). This is consistent with what
819   Miller et al. (2023) observed where the highest median levels of organic and elemental carbon
820   mass during CAMP^{2}Ex were due to biomass burning from the Maritime Continent. Without
821   organics, the baseline f(RH) (1.38 – 1.55, Fig. 4), is still relatively low, compared to measurements
822   from other areas (i.e. 2.19 from SEAC^{4}RS in and around the U.S.) (Shingler et al., 2016a) probably
823   due to the presence of elemental carbon, which is the second most dominant aerosol type during
824   the campaign.

825   Farther away from the Maritime Continent, the organic particles have aged and become more
826   oxidized as they interacted with the other air masses. The West Pacific is a relatively remote region
827   in northern Philippines and downwind of biomass burning from MC, creating a combined marine
828   and polluted aerosol. The oldest biomass burning aerosols were observed there. The organic
829   oxidation values of the aerosol particles in the air mass from the West Pacific are close to the
830   threshold of maximum oxidation that has been observed in previous studies (Cubison et al., 2011).
831   In the West Pacific, vertical transport decreases and increases hygroscopicity at cloud level with
832   increased organic and sulfate mass fractions, respectively. These aerosol constituents are thought
833   to be transported from the MC and the Philippines and their surrounding oceans, where natural
834   and industrial sources are significant (Miller et al., 2023), and then cloud processed.

835   Evaluation of the global chemical transport CAM-chem model at two output grids (~111 km and
836   25 km) against two convective cases from CAMP^{2}Ex show the underrepresentation of organics in
837   general and a higher derived aerosol hygroscopicity (kappa), which may be linked to the possible
838   overestimation of aerosol hygroscopicity from biomass burning from other studies in the area
839   (Collow et al., 2022; Edwards et al., 2022). CAM-chem overestimates sulfate in the tropical
840   cyclone induced convection case, consistent with results from an assessment of the NAAPS
841   reanalysis product on the positive bias of sulfate from East Asia (Edwards et al., 2022). The vertical
842   representation of the aerosol composition for the larger scale convection case due to a tropical
843   cyclone is better than that for the shallow convection case. Cloud processing and increased
844   hygroscopicity are not captured by the model for the shallow convection case, irrespective of
845   model grid size. The representation of shallow convection in the area by global models remains
846   challenging, based on similar model-evaluation studies (Collow et al., 2022). Past studies on
847   biomass burning aerosol effects on convection in Southeast Asia using a cloud-scale model

848 emphasized the importance of aerosol composition and absorptive properties, and their effect on
849 atmospheric stability, in the understanding of aerosol-cloud interactions (Hodzic and Duvel, 2018).
850 It is thus ideal that cloud-scale models be evaluated using the dataset from CAMP^{2}Ex, where the
851 invigoration of shallow clouds has been observed (Reid et al., 2023).

852 The implications of the low aerosol hygroscopicity in the region and its effects on clouds and
853 climate are just beginning to be unraveled. The mixing and aging of organic and elemental carbon
854 from biomass burning smoke in the Maritime Continent with background and transported sources
855 influences hygroscopicity observations and modeling uncertainties and can be the topic of future
856 work. Improvements in harmonization in terms of aerosol particle sizes and composition, along
857 with updated emissions inventories, will be helpful moving forward both for the observations and
858 modeling of aerosol hygroscopicity. These suggestions can hopefully improve shallow cumulus
859 representation, which is still the biggest source of differences in model sensitivity in the
860 understanding of climate change (Bony and Dufresne, 2005), in the region and globally. Emerging
861 endeavors to implement higher resolution schemes in a large domain (Pfister et al., 2020; Radtke
862 et al., 2021) to capture both fine scale aerosol-cloud processes along with improved observations
863 in Southeast Asia hold promise.

864

890

References

Adam, M. G., Tran, P. T., Bolan, N., and Balasubramanian, R.: Biomass burning-derived airborne particulate matter in Southeast Asia: A critical review, Journal of Hazardous Materials, 407, 124760, https://doi.org/10.1016/j.jhazmat.2020.124760, 2021.

Amnuaylojaroen, T.: Air Pollution Modeling in Southeast Asia—An Overview, Vegetation Fires and Pollution in Asia, 531-544, https://doi.org/10.1007/978-3-031-29916-2_31, 2023.

Anderson, T. L., and Ogren, J. A.: Determining aerosol radiative properties using the TSI 3563 integrating nephelometer, Aerosol Science and Technology, 29, 57-69, https://doi.org/10.1080/02786829808965551, 1998.

Ångström, A.: On the atmospheric transmission of sun radiation and on dust in the air, Geografiska Annaler, 11, 156-166, https://doi.org/10.1080/20014422.1929.11880498, 1929.

Attwood, A., Washenfelder, R., Brock, C., Hu, W., Baumann, K., Campuzano-Jost, P., Day, D., Edgerton, E., Murphy, D., and Palm, B.: Trends in sulfate and organic aerosol mass in the Southeast US: Impact on aerosol optical depth and radiative forcing, Geophysical Research Letters, 41, 7701-7709, https://doi.org/10.1002/2014GL061669, 2014.

AzadiAghdam, M., Braun, R. A., Edwards, E.-L., Bañaga, P. A., Cruz, M. T., Betito, G., Cambaliza, M. O., Dadashazar, H., Lorenzo, G. R., and Ma, L.: On the nature of sea salt aerosol at a coastal megacity: Insights from Manila, Philippines in Southeast Asia, Atmos. Environ., 216, 116922, https://doi.org/10.1016/j.atmosenv.2019.116922, 2019.

Barth, M., Rasch, P., Kiehl, J., Benkovitz, C., and Schwartz, S.: Sulfur chemistry in the National Center for Atmospheric Research Community Climate Model: Description, evaluation, features, and sensitivity to aqueous chemistry, J. Geophys. Res.- Atmos., 105, 1387-1415, https://doi.org/10.1029/1999JD900773, 2000.

Baynard, T., Garland, R., Ravishankara, A., Tolbert, M., and Lovejoy, E.: Key factors influencing the relative humidity dependence of aerosol light scattering, Geophysical research letters, 33, https://doi.org/10.1029/2005GL024898, 2006.

Bergstrom, R. W., Pilewskie, P., Russell, P. B., Redemann, J., Bond, T. C., Quinn, P. K., and Sierau, B.: Spectral absorption properties of atmospheric aerosols, Atmos. Chem. Phys., 7, 5937-5943, https://doi.org/10.5194/acp-7-5937-2007, 2007.

Bony, S., and Dufresne, J. L.: Marine boundary layer clouds at the heart of tropical cloud feedback uncertainties in climate models, Geophysical Research Letters, 32, https://doi.org/10.1029/2005GL023851, 2005.

Brock, C., Wagner, N., and Gordon, T.: Effect of Aerosol Size and Hygroscopicity on Aerosol Optical Depth in the Southeastern United States, EGU General Assembly Conference Abstracts, 2016a.

Brock, C. A., Wagner, N. L., Anderson, B. E., Attwood, A. R., Beyersdorf, A., Campuzano-Jost, P., Carlton, A. G., Day, D. A., Diskin, G. S., and Gordon, T. D.: Aerosol optical properties in the southeastern United States in summer-Part 1: Hygroscopic growth, https://doi.org/10.5194/acp-16-4987-2016, 2016b.

Brooks, S. D., Wise, M. E., Cushing, M., and Tolbert, M. A.: Deliquescence behavior of organic/ammonium sulfate aerosol, Geophysical Research Letters, 29, 23-21-23-24, https://doi.org/10.1029/2002GL014733, 2002.

933 Burgos, M. A., Andrews, E., Titos, G., Alados-Arboledas, L., Baltensperger, U., Day, D.,
934 Jefferson, A., Kalivitis, N., Mihalopoulos, N., and Sherman, J.: A global view on the effect of
935 water uptake on aerosol particle light scattering, Scientific data, 6, 1-19,
936 https://doi.org/10.1038/s41597-019-0158-7, 2019.
937 Cazorla, A., Bahadur, R., Suski, K., Cahill, J. F., Chand, D., Schmid, B., Ramanathan, V., and
938 Prather, K.: Relating aerosol absorption due to soot, organic carbon, and dust to emission sources
939 determined from in-situ chemical measurements, Atmospheric Chemistry and Physics, 13, 9337-
940 9350, https://doi.org/10.5194/acp-13-9337-2013, 2013.
941 Chandra, A. S., Zhang, C., Klein, S. A., and Ma, H. Y.: Low-cloud characteristics over the
942 tropical western Pacific from ARM observations and CAM5 simulations, Journal of Geophysical
943 Research: Atmospheres, 120, 8953-8970, https://doi.org/10.1002/2015JD023369, 2015.
944 Che, H., Segal-Rozenhaimer, M., Zhang, L., Dang, C., Zuidema, P., Dobracki, A., Sedlacek III,
945 A. J., Coe, H., Wu, H., and Taylor, J.: Cloud processing and weeklong ageing affect biomass
946 burning aerosol properties over the south-eastern Atlantic, Communications earth &
947 environment, 3, 182, https://doi.org/10.1038/s43247-022-00517-3, 2022.
948 Chen, J., Zhao, C., Ma, N., and Yan, P.: Aerosol hygroscopicity parameter derived from the light
949 scattering enhancement factor measurements in the North China Plain, Atmospheric Chemistry
950 and Physics, 14, 8105-8118, https://doi.org/10.5194/acp-14-8105-2014, 2014.
951 Chen, J., Budisulistiorini, S. H., Itoh, M., and Kuwata, M.: Roles of relative humidity and
952 particle size on chemical aging of tropical peatland burning particles: Potential influence of
953 phase state and implications for hygroscopic property, Journal of Geophysical Research:
954 Atmospheres, 127, e2022JD036871, https://doi.org/10.1029/2022JD036871, 2022.
955 Chen, Q., McGowan, S., Gouramanis, C., Fong, L., Balasubramanian, R., and Taylor, D.:
956 Rapidly rising transboundary atmospheric pollution from industrial and urban sources in
957 Southeast Asia and its implications for regional sustainable development, Environ. Res. Lett., 15,
958 1040a1045, https://doi.org/10.1088/1748-9326/abb5ce, 2020.
959 Collow, A. B. M., Buchard, V., Colarco, P. R., da Silva, A. M., Govindaraju, R., Nowottnick, E.
960 P., Burton, S., Ferrare, R., Hostetler, C., and Ziemba, L.: An evaluation of biomass burning
961 aerosol mass, extinction, and size distribution in GEOS using observations from CAMP 2 Ex,
962 Atmospheric Chemistry and Physics, 22, 16091-16109, https://doi.org/10.5194/acp-22-16091-
963 2022, 2022.
964 Covert, D. S., Charlson, R., and Ahlquist, N.: A study of the relationship of chemical
965 composition and humidity to light scattering by aerosols, Journal of Applied Meteorology, 11,
966 968-976, https://doi.org/10.1175/1520-0450(1972)011<0968:ASOTRO>2.0.CO;2, 1972.
967 Crosbie, E., Ziemba, L. D., Shook, M. A., Robinson, C. E., Winstead, E. L., Thornhill, K. L.,
968 Braun, R. A., MacDonald, A. B., Stahl, C., and Sorooshian, A.: Measurement report: Closure
969 analysis of aerosol–cloud composition in tropical maritime warm convection, Atmos. Chem.
970 Phys., 22, 13269-13302, https://doi.org/10.5194/acp-22-13269-2022, 2022.
971 Crumeyrolle, S., Gomes, L., Tulet, P., Matsuki, A., Schwarzenboeck, A., and Crahan, K.:
972 Increase of the aerosol hygroscopicity by cloud processing in a mesoscale convective system: a
973 case study from the AMMA campaign, Atmospheric Chemistry and Physics, 8, 6907-6924,
974 https://doi.org/10.5194/acp-8-6907-2008, 2008.
975 Cruz, M. T., Bañaga, P. A., Betito, G., Braun, R. A., Stahl, C., Aghdam, M. A., Cambaliza, M.
976 O., Dadashazar, H., Hilario, M. R., Lorenzo, G. R., Ma, L., MacDonald, A. B., Pabroa, C., Yee,
977 J. R., Simpas, J. B., and Sorooshian, A.: Size-resolved composition and morphology of

978   particulate matter during the southwest monsoon in Metro Manila, Philippines, Atmos. Chem.
979   Phys., 19, 10675–10696, https://doi.org/10.5194/acp-19-10675-2019, 2019.
980   Cubison, M., Ortega, A., Hayes, P., Farmer, D., Day, D., Lechner, M., Brune, W., Apel, E.,
981   Diskin, G., and Fisher, J.: Effects of aging on organic aerosol from open biomass burning smoke
982   in aircraft and laboratory studies, Atmospheric Chemistry and Physics, 11, 12049-12064,
983   https://doi.org/10.5194/acp-11-12049-2011, 2011.
984   Dadashazar, H., Corral, A. F., Crosbie, E., Dmitrovic, S., Kirschler, S., McCauley, K., Moore,
985   R., Robinson, C., Schlosser, J. S., and Shook, M.: Organic enrichment in droplet residual
986   particles relative to out of cloud over the northwestern Atlantic: analysis of airborne ACTIVATE
987   data, Atmospheric Chemistry and Physics, 22, 13897-13913, https://doi.org/10.5194/acp-22-
988   13897-2022, 2022.
989   Dockery, D. W.: Epidemiologic evidence of cardiovascular effects of particulate air pollution,
990   Environmental health perspectives, 109, 483-486, https://doi.org/10.1289/ehp.01109s4483, 2001.
991   Dong, X., Fu, J. S., Huang, K., Lin, N.-H., Wang, S.-H., and Yang, C.-E.: Analysis of the co-
992   existence of long-range transport biomass burning and dust in the subtropical West Pacific
993   Region, Scientific Reports, 8, 8962, https://doi.org/10.1038/s41598-018-27129-2, 2018.
994   Dubovik, O., Holben, B., Eck, T. F., Smirnov, A., Kaufman, Y. J., King, M. D., Tanré, D., and
995   Slutsker, I.: Variability of absorption and optical properties of key aerosol types observed in
996   worldwide locations, J. Atmos. Sci., 59, 590-608, https://doi.org/10.1175/1520-
997   0469(2002)059<0590:VOAAOP>2.0.CO;2, 2002.
998   Duplissy, J., DeCarlo, P. F., Dommen, J., Alfarra, M. R., Metzger, A., Barmpadimos, I., Prevot,
999   A. S., Weingartner, E., Tritscher, T., and Gysel, M.: Relating hygroscopicity and composition of
1000   organic aerosol particulate matter, Atmospheric Chemistry and Physics, 11, 1155-1165,
1001   https://doi.org/10.5194/acp-11-1155-2011, 2011.
1002   Eck, T. F., Holben, B. N., Reid, J., Giles, D., Rivas, M., Singh, R. P., Tripathi, S., Bruegge, C.,
1003   Platnick, S., and Arnold, G.: Fog-and cloud-induced aerosol modification observed by the
1004   Aerosol Robotic Network (AERONET), J. Geophys. Res.- Atmos., 117,
1005   https://doi.org/10.1029/2011JD016839, 2012.
1006   Edwards, E.-L., Reid, J. S., Xian, P., Burton, S. P., Cook, A. L., Crosbie, E. C., Fenn, M. A.,
1007   Ferrare, R. A., Freeman, S. W., and Hair, J. W.: Assessment of NAAPS-RA performance in
1008   Maritime Southeast Asia during CAMP 2 Ex, Atmospheric Chemistry and Physics, 22, 12961-
1009   12983, https://doi.org/10.5194/acp-22-12961-2022, 2022.
1010   Engelhart, G., Asa-Awuku, A., Nenes, A., and Pandis, S.: CCN activity and droplet growth
1011   kinetics of fresh and aged monoterpene secondary organic aerosol, Atmospheric Chemistry and
1012   Physics, 8, 3937-3949, https://doi.org/10.5194/acp-8-3937-2008, 2008.
1013   Faloona, I.: Sulfur processing in the marine atmospheric boundary layer: A review and critical
1014   assessment of modeling uncertainties, Atmos. Environ., 43, 2841-2854,
1015   https://doi.org/10.1016/j.atmosenv.2009.02.043, 2009.
1016   Fan, X., Liu, J., Zhang, F., Chen, L., Collins, D., Xu, W., Jin, X., Ren, J., Wang, Y., and Wu, H.:
1017   Contrasting size-resolved hygroscopicity of fine particles derived by HTDMA and HR-ToF-
1018   AMS measurements between summer and winter in Beijing: the impacts of aerosol aging and
1019   local emissions, Atmospheric Chemistry and Physics, 20, 915-929, https://doi.org/10.5194/acp-
1020   20-915-2020, 2020.
1021   Ferrare, R., Melfi, S., Whiteman, D., Evans, K., Poellot, M., and Kaufman, Y.: Raman lidar
1022   measurements of aerosol extinction and backscattering: 2. Derivation of aerosol real refractive
1023   index, single-scattering albedo, and humidification factor using Raman lidar and aircraft size

distribution measurements, Journal of Geophysical Research: Atmospheres, 103, 19673-19689, https://doi.org/10.1029/98JD01647, 1998.

Ferrare, R., Hair, J., Hostetler, C., Shingler, T., Burton, S. P., Fenn, M., Clayton, M., Scarino, A. J., Harper, D., and Seaman, S.: Airborne HSRL-2 measurements of elevated aerosol depolarization associated with non-spherical sea salt, Frontiers in Remote Sensing, 4, 1143944, https://doi.org/10.3389/frsen.2023.1143944, 2023.

Garland, R. M., Ravishankara, A., Lovejoy, E. R., Tolbert, M. A., and Baynard, T.: Parameterization for the relative humidity dependence of light extinction: Organic-ammonium sulfate aerosol, Journal of Geophysical Research: Atmospheres, 112, https://doi.org/10.1029/2006JD008179, 2007.

Garofalo, L. A., Pothier, M. A., Levin, E. J., Campos, T., Kreidenweis, S. M., and Farmer, D. K.: Emission and evolution of submicron organic aerosol in smoke from wildfires in the western United States, ACS Earth and Space Chemistry, 3, 1237-1247, https://doi.org/10.1021/acsearthspacechem.9b00125, 2019.

Gasparini, R., Collins, D. R., Andrews, E., Sheridan, P. J., Ogren, J. A., and Hudson, J. G.: Coupling aerosol size distributions and size-resolved hygroscopicity to predict humidity-dependent optical properties and cloud condensation nuclei spectra, Journal of Geophysical Research: Atmospheres, 111, https://doi.org/10.1029/2005JD006092, 2006.

Hänel, G.: The properties of atmospheric aerosol particles as functions of the relative humidity at thermodynamic equilibrium with the surrounding moist air, in: Advances in geophysics, Elsevier, 73-188, 1976.

Hegg, D., Larson, T., and Yuen, P. F.: A theoretical study of the effect of relative humidity on light scattering by tropospheric aerosols, Journal of Geophysical Research: Atmospheres, 98, 18435-18439, https://doi.org/10.1029/93JD01928, 1993.

Hilario, M. R., Barth, M. C., Crosbie, E., Lorenzo, G. R., Rutledge, S. A., Wang, J., Xiao, Q., Ziemba, L. D., and Sorooshian, A.: Quantifying scavenging efficiencies of different aerosol species and size-resolved volume concentrations in tropical convective clouds over the West Pacific, AGU Fall Meeting Abstracts, 2023, A41M-2809.

Hilario, M. R. A., Crosbie, E., Shook, M., Reid, J. S., Cambaliza, M. O. L., Simpas, J. B. B., Ziemba, L., DiGangi, J. P., Diskin, G. S., and Nguyen, P.: Measurement report: Long-range transport patterns into the tropical northwest Pacific during the CAMP²Ex aircraft campaign: chemical composition, size distributions, and the impact of convection, Atmos. Chem. Phys., 21, 3777-3802, https://doi.org/10.5194/acp-21-3777-2021, 2021.

Hodzic, A., and Duvel, J. P.: Impact of biomass burning aerosols on the diurnal cycle of convective clouds and precipitation over a tropical island, Journal of Geophysical Research: Atmospheres, 123, 1017-1036, https://doi.org/10.1002/2017JD027521, 2018.

Hong, Y., and Di Girolamo, L.: Cloud phase characteristics over Southeast Asia from A-Train satellite observations, Atmos. Chem. Phys., 20, 8267-8291, https://doi.org/10.5194/acp-20-8267-2020, 2020.

Höpner, F., Bender, F. M., Ekman, A. M., Andersson, A., Gustafsson, Ö., and Leck, C.: Investigation of two optical methods for aerosol-type classification extended to a Northern Indian Ocean site, Journal of Geophysical Research: Atmospheres, 124, 8743-8763, https://doi.org/10.1029/2018JD029685, 2019.

Kalberer, M.: Aerosol physics and chemistry, Encyclopedia of Atmospheric Sciences, 1, 23, 2014.

1069 Kar, J., Bremer, H., Drummond, J. R., Rochon, Y. J., Jones, D. B., Nichitiu, F., Zou, J., Liu, J.,
1070 Gille, J. C., and Edwards, D. P.: Evidence of vertical transport of carbon monoxide from
1071 Measurements of Pollution in the Troposphere (MOPITT), Geophysical research letters, 31,
1072 2004.
1073 Kavouras, I. G., Nikolich, G., Etyemezian, V., DuBois, D. W., King, J., and Shafer, D.: In situ
1074 observations of soil minerals and organic matter in the early phases of prescribed fires, Journal of
1075 Geophysical Research: Atmospheres, 117, https://doi.org/10.1029/2011JD017420, 2012.
1076 Köhler, H.: The nucleus in and the growth of hygroscopic droplets, Transactions of the Faraday
1077 Society, 32, 1152-1161, 1936.
1078 Kreidenweis, S., and Asa-Awuku, A.: Aerosol Hygroscopicity: Particle water content and its role
1079 in atmospheric processes, https://doi.org/10.1016/B978-0-08-095975-7.00418-6, 2014.
1080 Kuang, Y., Zhao, C., Tao, J., Bian, Y., Ma, N., and Zhao, G.: A novel method for deriving the
1081 aerosol hygroscopicity parameter based only on measurements from a humidified nephelometer
1082 system, Atmospheric Chemistry and Physics, 17, 6651-6662, https://doi.org/10.5194/acp-17-
1083 6651-2017, 2017.
1084 Kuang, Y., He, Y., Xu, W., Zhao, P., Cheng, Y., Zhao, G., Tao, J., Ma, N., Su, H., and Zhang,
1085 Y.: Distinct diurnal variation in organic aerosol hygroscopicity and its relationship with
1086 oxygenated organic aerosol, Atmospheric Chemistry and Physics, 20, 865-880, 2020.
1087 Lacagnina, C., Hasekamp, O. P., Bian, H., Curci, G., Myhre, G., van Noije, T., Schulz, M.,
1088 Skeie, R. B., Takemura, T., and Zhang, K.: Aerosol single-scattering albedo over the global
1089 oceans: Comparing PARASOL retrievals with AERONET, OMI, and AeroCom models
1090 estimates, Journal of Geophysical Research: Atmospheres, 120, 9814-9836,
1091 https://doi.org/10.1002/2015JD023501, 2015.
1092 Lee, H.-H., Iraqui, O., Gu, Y., Yim, S. H.-L., Chulakadabba, A., Tonks, A. Y.-M., Yang, Z., and
1093 Wang, C.: Impacts of air pollutants from fire and non-fire emissions on the regional air quality in
1094 Southeast Asia, Atmos. Chem. Phys., 18, 6141-6156, https://doi.org/10.5194/acp-18-6141-2018,
1095 2018.
1096 Li, G., Bei, N., Cao, J., Huang, R., Wu, J., Feng, T., Wang, Y., Liu, S., Zhang, Q., and Tie, X.: A
1097 possible pathway for rapid growth of sulfate during haze days in China, Atmos. Chem. Phys., 17,
1098 3301-3316, https://doi.org/10.5194/acp-17-3301-2017, 2017.
1099 Liu, H., Zhao, C., Nekat, B., Ma, N., Wiedensohler, A., Van Pinxteren, D., Spindler, G., Müller,
1100 K., and Herrmann, H.: Aerosol hygroscopicity derived from size-segregated chemical
1101 composition and its parameterization in the North China Plain, Atmospheric Chemistry and
1102 Physics, 14, 2525-2539, https://doi.org/10.5194/acp-14-2525-2014, 2014.
1103 Liu, X., Ma, P.-L., Wang, H., Tilmes, S., Singh, B., Easter, R., Ghan, S., and Rasch, P.:
1104 Description and evaluation of a new four-mode version of the Modal Aerosol Module (MAM4)
1105 within version 5.3 of the Community Atmosphere Model, Geoscientific Model Development, 9,
1106 505-522, https://doi.org/10.5194/gmd-9-505-2016, 2016.
1107 Lorenzo, G. R., Arellano, A. F., Cambaliza, M. O., Castro, C., Cruz, M. T., Di Girolamo, L.,
1108 Gacal, G. F., Hilario, M. R. A., Lagrosas, N., Ong, H. J., Simpas, J. B., Uy, S. N., and
1109 Sorooshian, A.: An emerging aerosol climatology via remote sensing over Metro Manila, the
1110 Philippines, Atmospheric Chemistry and Physics, 23, 10579-10608, https://doi.org/10.5194/acp-
1111 23-10579-2023, 2023.
1112 Malm, W. C., and Day, D. E.: Estimates of aerosol species scattering characteristics as a function
1113 of relative humidity, Atmospheric Environment, 35, 2845-2860, https://doi.org/10.1016/S1352-
1114 2310(01)00077-2, 2001.

1115 Mason, B., Wagner, N., Adler, G., Andrews, E., Brock, C., Gordon, T., Lack, D., Perring, A.,
1116 Richardson, M., and Schwarz, J.: An intercomparison of aerosol absorption measurements
1117 conducted during the SEAC4RS campaign, Aerosol Science and Technology, 52, 1012-1027,
1118 https://doi.org/10.1080/02786826.2018.1500012, 2018.
1119 Maudlin, L., Wang, Z., Jonsson, H., and Sorooshian, A.: Impact of wildfires on size-resolved
1120 aerosol composition at a coastal California site, Atmospheric Environment, 119, 59-68,
1121 https://doi.org/10.1016/j.atmosenv.2015.08.039, 2015.
1122 McNaughton, C. S., Clarke, A. D., Howell, S. G., Pinkerton, M., Anderson, B., Thornhill, L.,
1123 Hudgins, C., Winstead, E., Dibb, J. E., and Scheuer, E.: Results from the DC-8 Inlet
1124 Characterization Experiment (DICE): Airborne versus surface sampling of mineral dust and sea
1125 salt aerosols, Aerosol Science and Technology, 41, 136-159,
1126 https://doi.org/10.1080/02786820601118406, 2007.
1127 Miller, R. M., Rauber, R. M., Di Girolamo, L., Rilloraza, M., Fu, D., McFarquhar, G. M.,
1128 Nesbitt, S. W., Ziemba, L. D., Woods, S., and Thornhill, K. L.: Influence of natural and
1129 anthropogenic aerosols on cloud base droplet size distributions in clouds over the South China
1130 Sea and West Pacific, Atmospheric Chemistry and Physics, 23, 8959-8977,
1131 https://doi.org/10.5194/acp-23-8959-2023, 2023.
1132 Mochida, M., Kuwata, M., Miyakawa, T., Takegawa, N., Kawamura, K., and Kondo, Y.:
1133 Relationship between hygroscopicity and cloud condensation nuclei activity for urban aerosols in
1134 Tokyo, Journal of Geophysical Research: Atmospheres, 111,
1135 https://doi.org/10.1029/2005JD006980, 2006.
1136 Moosmüller, H., and Sorensen, C.: Small and large particle limits of single scattering albedo for
1137 homogeneous, spherical particles, J. Quant. Spectrosc. Ra., 204, 250-255,
1138 https://doi.org/10.1016/j.jqsrt.2017.09.029, 2018.
1139 Nakajima, T., Higurashi, A., Takeuchi, N., and Herman, J. R.: Satellite and ground-based study
1140 of optical properties of 1997 Indonesian forest fire aerosols, Geophysical Research Letters, 26,
1141 2421-2424, https://doi.org/10.1029/1999GL900208, 1999.
1142 NASA, E. D.: Fires in Kalimantan, Indonesia, in, Worldview Image of the Week, 2020.
1143 Oanh, N. K., Upadhyay, N., Zhuang, Y.-H., Hao, Z.-P., Murthy, D., Lestari, P., Villarin, J.,
1144 Chengchua, K., Co, H., and Dung, N.: Particulate air pollution in six Asian cities: Spatial and
1145 temporal distributions, and associated sources, Atmospheric environment, 40, 3367-3380,
1146 https://doi.org/10.1016/j.atmosenv.2006.01.050, 2006.
1147 Othman, M., Latif, M. T., Hamid, H. H. A., Uning, R., Khumsaeng, T., Phairuang, W., Daud, Z.,
1148 Idris, J., Sofwan, N. M., and Lung, S.-C. C.: Spatial–temporal variability and health impact of
1149 particulate matter during a 2019–2020 biomass burning event in Southeast Asia, Scientific
1150 Reports, 12, 7630, https://doi.org/10.1038/s41598-022-11409-z, 2022.
1151 Palmer, T. Y.: Large fire winds, gases and smoke, Atmospheric Environment (1967), 15, 2079-
1152 2090, https://doi.org/10.1016/0004-6981(81)90241-9, 1981.
1153 Pawar, P. V., Ghude, S. D., Jena, C., Móring, A., Sutton, M. A., Kulkarni, S., Lal, D. M.,
1154 Surendran, D., Van Damme, M., and Clarisse, L.: Analysis of atmospheric ammonia over South
1155 and East Asia based on the MOZART-4 model and its comparison with satellite and surface
1156 observations, Atmospheric Chemistry and Physics, 21, 6389-6409, https://doi.org/10.5194/acp-
1157 21-6389-2021, 2021.
1158 Petters, M., and Kreidenweis, S.: A single parameter representation of hygroscopic growth and
1159 cloud condensation nucleus activity, Atmospheric Chemistry and Physics, 7, 1961-1971,
1160 https://doi.org/10.5194/acp-7-1961-2007, 2007.

1161   Pfister, G. G., Eastham, S. D., Arellano, A. F., Aumont, B., Barsanti, K. C., Barth, M. C.,
1162   Conley, A., Davis, N. A., Emmons, L. K., and Fast, J. D.: The multi-scale infrastructure for
1163   chemistry and aerosols (MUSICA), Bulletin of the American Meteorological Society, 101,
1164   E1743-E1760, https://doi.org/10.1175/BAMS-D-19-0331.1, 2020.
1165   Pokhrel, R. P., Gordon, J., Fiddler, M. N., and Bililign, S.: Impact of combustion conditions on
1166   physical and morphological properties of biomass burning aerosol, Aerosol Science and
1167   Technology, 55, 80-91, https://doi.org/10.1080/02786826.2020.1822512, 2021.
1168   Pringle, K., Tost, H., Pozzer, A., Pöschl, U., and Lelieveld, J.: Global distribution of the effective
1169   aerosol hygroscopicity parameter for CCN activation, Atmospheric Chemistry and Physics, 10,
1170   5241-5255, https://doi.org/10.5194/acp-10-5241-2010, 2010.
1171   Radtke, J., Mauritsen, T., and Hohenegger, C.: Shallow cumulus cloud feedback in large eddy
1172   simulations–bridging the gap to storm-resolving models, Atmospheric Chemistry and Physics,
1173   21, 3275-3288, https://doi.org/10.5194/acp-21-3275-2021, 2021.
1174   Reid, J., Koppmann, R., Eck, T., and Eleuterio, D.: A review of biomass burning emissions part
1175   II: intensive physical properties of biomass burning particles, Atmos. Chem. Phys., 5, 799-825,
1176   https://doi.org/10.5194/acp-5-799-2005, 2005.
1177   Reid, J., Maring, H., Narisma, G., van den Heever, S., Di Girolamo, L., Ferrare, R., Holz, R.,
1178   Lawson, P., Mace, G., and Simpas, J.: The coupling between tropical meteorology, aerosol
1179   lifecycle, convection, and radiation, during the Cloud, Aerosol and Monsoon Processes
1180   Philippines Experiment (CAMP 2 Ex), B. Am. Meteorol. Soc., https://doi.org/10.1175/BAMS-
1181   D-21-0285.1, 2023.
1182   Reid, J. S., Hyer, E. J., Johnson, R. S., Holben, B. N., Yokelson, R. J., Zhang, J., Campbell, J. R.,
1183   Christopher, S. A., Di Girolamo, L., and Giglio, L.: Observing and understanding the Southeast
1184   Asian aerosol system by remote sensing: An initial review and analysis for the Seven Southeast
1185   Asian Studies (7SEAS) program, Atmos. Res., 122, 403-468,
1186   https://doi.org/10.1016/j.atmosres.2012.06.005, 2013.
1187   Robinson, M. S., Chavez, J., Velazquez, S., and Jayanty, R.: Chemical speciation of PM2. 5
1188   collected during prescribed fires of the Coconino National Forest near Flagstaff, Arizona, Journal
1189   of the Air & Waste Management Association, 54, 1112-1123,
1190   https://doi.org/10.1080/10473289.2004.10470985, 2004.
1191   Rolph, G., Stein, A., and Stunder, B.: Real-time environmental applications and display system:
1192   READY, Environ. Modell. Softw., 95, 210-228, https://doi.org/10.1016/j.envsoft.2017.06.025,
1193   2017.
1194   Ross, A. D., Holz, R. E., Quinn, G., Reid, J. S., Xian, P., Turk, F. J., and Posselt, D. J.: Exploring
1195   the first aerosol indirect effect over Southeast Asia using a 10-year collocated MODIS, CALIOP,
1196   and model dataset, Atmospheric Chemistry and Physics, 18, 12747-12764,
1197   https://doi.org/10.5194/acp-18-12747-2018, 2018.
1198   Saxena, P., Hildemann, L. M., McMurry, P. H., and Seinfeld, J. H.: Organics alter hygroscopic
1199   behavior of atmospheric particles, Journal of Geophysical Research: Atmospheres, 100, 18755-
1200   18770, https://doi.org/10.1029/95JD01835, 1995.
1201   Schlosser, J. S., Braun, R. A., Bradley, T., Dadashazar, H., MacDonald, A. B., Aldhaif, A. A.,
1202   Aghdam, M. A., Mardi, A. H., Xian, P., and Sorooshian, A.: Analysis of aerosol composition
1203   data for western United States wildfires between 2005 and 2015: Dust emissions, chloride
1204   depletion, and most enhanced aerosol constituents, J. Geophys. Res.- Atmos., 122, 8951-8966,
1205   https://doi.org/10.1002/2017JD026547, 2017.

1206   Schuster, G. L., Dubovik, O., and Holben, B. N.: Angstrom exponent and bimodal aerosol size
1207   distributions, J. Geophys. Res.- Atmos., 111, https://doi.org/10.1029/2005JD006328, 2006.
1208   Schwantes, R. H., Lacey, F. G., Tilmes, S., Emmons, L. K., Lauritzen, P. H., Walters, S.,
1209   Callaghan, P., Zarzycki, C. M., Barth, M. C., and Jo, D. S.: Evaluating the impact of chemical
1210   complexity and horizontal resolution on tropospheric ozone over the conterminous US with a
1211   global variable resolution chemistry model, Journal of Advances in Modeling Earth Systems, 14,
1212   e2021MS002889, https://doi.org/10.1029/2021MS002889, 2022.
1213   Shi, J., Hong, J., Ma, N., Luo, Q., He, Y., Xu, H., Tan, H., Wang, Q., Tao, J., and Zhou, Y.:
1214   Measurement report: On the difference in aerosol hygroscopicity between high and low relative
1215   humidity conditions in the North China Plain, Atmospheric Chemistry and Physics, 22, 4599-
1216   4613, https://doi.org/10.5194/acp-22-4599-2022, 2022.
1217   Shingler, T., Crosbie, E., Ortega, A., Shiraiwa, M., Zuend, A., Beyersdorf, A., Ziemba, L.,
1218   Anderson, B., Thornhill, L., and Perring, A. E.: Airborne characterization of subsaturated aerosol
1219   hygroscopicity and dry refractive index from the surface to 6.5 km during the SEAC4RS
1220   campaign, Journal of Geophysical Research: Atmospheres, 121, 4188-4210,
1221   https://doi.org/10.1002/2015JD024498, 2016a.
1222   Shingler, T., Sorooshian, A., Ortega, A., Crosbie, E., Wonaschütz, A., Perring, A. E.,
1223   Beyersdorf, A., Ziemba, L., Jimenez, J. L., and Campuzano-Jost, P.: Ambient observations of
1224   hygroscopic growth factor and f (RH) below 1: Case studies from surface and airborne
1225   measurements, Journal of Geophysical Research: Atmospheres, 121, 13,661-613,677,
1226   https://doi.org/10.1002/2016JD025471, 2016b.
1227   Smith, S. J., Aardenne, J. v., Klimont, Z., Andres, R. J., Volke, A., and Delgado Arias, S.:
1228   Anthropogenic sulfur dioxide emissions: 1850–2005, Atmos. Chem. Phys., 11, 1101-1116,
1229   https://doi.org/10.5194/acp-11-1101-2011, 2011.
1230   Sorooshian, A., Shingler, T., Crosbie, E., Barth, M., Homeyer, C., Campuzano-Jost, P., Day, D.,
1231   Jimenez, J., Thornhill, K., and Ziemba, L.: Contrasting aerosol refractive index and
1232   hygroscopicity in the inflow and outflow of deep convective storms: Analysis of airborne data
1233   from DC3, Journal of Geophysical Research: Atmospheres, 122, 4565-4577,
1234   https://doi.org/10.1002/2017JD026638, 2017.
1235   Spill, G., Stier, P., Field, P. R., and Dagan, G.: Effects of aerosol in simulations of realistic
1236   shallow cumulus cloud fields in a large domain, Atmospheric Chemistry and Physics, 19, 13507-
1237   13517, https://doi.org/10.5194/acp-19-13507-2019, 2019.
1238   Stein, A., Draxler, R. R., Rolph, G. D., Stunder, B. J., Cohen, M., and Ngan, F.: NOAA's
1239   HYSPLIT atmospheric transport and dispersion modeling system, B. Am. Meteorol. Soc., 96,
1240   2059-2077, https://doi.org/10.1175/BAMS-D-14-00110.1, 2015.
1241   Stockwell, C. E., Jayarathne, T., Cochrane, M. A., Ryan, K. C., Putra, E. I., Saharjo, B. H.,
1242   Nurhayati, A. D., Albar, I., Blake, D. R., and Simpson, I. J.: Field measurements of trace gases
1243   and aerosols emitted by peat fires in Central Kalimantan, Indonesia, during the 2015 El Niño,
1244   Atmospheric Chemistry and Physics, 16, 11711-11732, https://doi.org/10.5194/acp-16-11711-
1245   2016, 2016.
1246   Stokes, R., and Robinson, R.: Interactions in aqueous nonelectrolyte solutions. I. Solute-solvent
1247   equilibria, The Journal of Physical Chemistry, 70, 2126-2131, 1966.
1248   Swietlicki, E., Hansson, H.-C., Hämeri, K., Svenningsson, B., Massling, A., McFiggans, G.,
1249   McMurry, P. H., Petäjä, T., Tunved, P., and Gysel, M.: Hygroscopic properties of submicrometer
1250   atmospheric aerosol particles measured with H-TDMA instruments in various environments—a

review, Tellus B: Chemical and Physical Meteorology, 60, 432-469,
https://doi.org/10.1111/j.1600-0889.2008.00350.x, 2008.

Thalman, R., de Sá, S. S., Palm, B. B., Barbosa, H. M., Pöhlker, M. L., Alexander, M. L., Brito,
J., Carbone, S., Castillo, P., and Day, D. A.: CCN activity and organic hygroscopicity of aerosols
downwind of an urban region in central Amazonia: seasonal and diel variations and impact of
anthropogenic emissions, Atmospheric Chemistry and Physics, 17, 11779-11801,
https://doi.org/10.5194/acp-17-11779-2017, 2017.

Tilmes, S., Mills, M. J., Zhu, Y., Bardeen, C. G., Vitt, F., Yu, P., Fillmore, D., Liu, X., Toon, B.,
and Deshler, T.: Description and performance of a sectional aerosol microphysical model in the
Community Earth System Model (CESM2), Geoscientific Model Development, 16, 6087-6125,
https://doi.org/10.5194/gmd-16-6087-2023, 2023.

Titos, G., Burgos, M. A., Zieger, P., Alados-Arboledas, L., Baltensperger, U., Jefferson, A.,
Sherman, J., Weingartner, E., Henzing, B., and Luoma, K.: A global study of hygroscopicity-
driven light-scattering enhancement in the context of other in situ aerosol optical properties,
Atmospheric Chemistry and Physics, 21, 13031-13050, https://doi.org/10.5194/acp-21-13031-
2021, 2021.

Tsay, S.-C., Hsu, N. C., Lau, W. K.-M., Li, C., Gabriel, P. M., Ji, Q., Holben, B. N., Welton, E.
J., Nguyen, A. X., and Janjai, S.: From BASE-ASIA toward 7-SEAS: A satellite-surface
perspective of boreal spring biomass-burning aerosols and clouds in Southeast Asia,
Atmospheric environment, 78, 20-34, https://doi.org/10.1016/j.atmosenv.2012.12.013, 2013.

van Diedenhoven, B., Hasekamp, O. P., Cairns, B., Schuster, G. L., Stamnes, S., Shook, M., and
Ziemba, L.: Remote sensing of aerosol water fraction, dry size distribution and soluble fraction
using multi-angle, multi-spectral polarimetry, Atmospheric Measurement Techniques, 15, 7411-
7434, https://doi.org/10.5194/amt-15-7411-2022, 2022.

Virkkula, A.: Correction of the calibration of the 3-wavelength Particle Soot Absorption
Photometer (3λ PSAP), Aerosol Science and Technology, 44, 706-712,
https://doi.org/10.1080/02786826.2010.482110, 2010.

Waggoner, A., Weiss, R., and Larson, T.: In-situ, rapid response measurement of H2SO4/(NH4)
2SO4 aerosols in urban Houston: A comparison with rural Virginia, Atmospheric Environment
(1967), 17, 1723-1731, https://doi.org/10.1016/0004-6981(83)90179-8, 1983.

Wang, X., Ye, X., Chen, H., Chen, J., Yang, X., and Gross, D. S.: Online hygroscopicity and
chemical measurement of urban aerosol in Shanghai, China, Atmospheric Environment, 95, 318-
326, https://doi.org/10.1016/j.atmosenv.2014.06.051, 2014.

Wang, Y., Li, Z., Zhang, Y., Du, W., Zhang, F., Tan, H., Xu, H., Fan, T., Jin, X., and Fan, X.:
Characterization of aerosol hygroscopicity, mixing state, and CCN activity at a suburban site in
the central North China Plain, Atmospheric Chemistry and Physics, 18, 11739-11752,
https://doi.org/10.5194/acp-18-11739-2018, 2018.

Wu, Z., Zheng, J., Shang, D., Du, Z., Wu, Y., Zeng, L., Wiedensohler, A., and Hu, M.: Particle
hygroscopicity and its link to chemical composition in the urban atmosphere of Beijing, China,
during summertime, Atmospheric Chemistry and Physics, 16, 1123-1138,
https://doi.org/10.5194/acp-16-1123-2016, 2016.

Xu, W., Ovadnevaite, J., Fossum, K. N., Lin, C., Huang, R.-J., O'Dowd, C., and Ceburnis, D.:
Aerosol hygroscopicity and its link to chemical composition in the coastal atmosphere of Mace
Head: marine and continental air masses, Atmospheric Chemistry and Physics, 20, 3777-3791,
https://doi.org/10.5194/acp-20-3777-2020, 2020.

1296   Yang, Q., Easter, R. C., Campuzano-Jost, P., Jimenez, J. L., Fast, J. D., Ghan, S. J., Wang, H.,
1297   Berg, L. K., Barth, M. C., and Liu, Y.: Aerosol transport and wet scavenging in deep convective
1298   clouds: A case study and model evaluation using a multiple passive tracer analysis approach,
1299   Journal of Geophysical Research: Atmospheres, 120, 8448-8468,
1300   https://doi.org/10.1002/2015JD023647, 2015.
1301   Zhang, F., Wang, Y., Peng, J., Ren, J., Collins, D., Zhang, R., Sun, Y., Yang, X., and Li, Z.:
1302   Uncertainty in predicting CCN activity of aged and primary aerosols, Journal of Geophysical
1303   Research: Atmospheres, 122, 11,723-711,736, https://doi.org/10.1002/2017JD027058, 2017.
1304   Zhao, G., Zhao, C., Kuang, Y., Bian, Y., Tao, J., Shen, C., and Yu, Y.: Calculating the aerosol
1305   asymmetry factor based on measurements from the humidified nephelometer system, Atmos.
1306   Chem. Phys., 18, 9049-9060, https://doi.org/10.5194/acp-18-9049-2018, 2018.
1307   Zieger, P., Fierz-Schmidhauser, R., Weingartner, E., and Baltensperger, U.: Effects of relative
1308   humidity on aerosol light scattering: results from different European sites, Atmospheric
1309   Chemistry and Physics, 13, 10609-10631, https://doi.org/10.5194/acp-13-10609-2013, 2013.
1310   Ziemba, L. D., Lee Thornhill, K., Ferrare, R., Barrick, J., Beyersdorf, A. J., Chen, G.,
1311   Crumeyrolle, S. N., Hair, J., Hostetler, C., and Hudgins, C.: Airborne observations of aerosol
1312   extinction by in situ and remote-sensing techniques: Evaluation of particle hygroscopicity,
1313   Geophysical Research Letters, 40, 417-422, https://doi.org/10.1029/2012GL054428, 2013.